

Vibrational Properties of Disordered Carbon Nanotube

By

Ashrafal Hossain Howlader

A thesis submitted in partial fulfillment of the requirements for the degree of
Master of Science
in Electrical and Electronic Engineering



Khulna University of Engineering & Technology

Khulna 9203, Bangladesh

October 2017

Declaration

This is to certify that the thesis work entitled "*Vibrational Properties of Disordered Carbon Nanotube*" has been carried out by *Ashraf Hossain Howlader* in the Department of *Electrical and Electronic Engineering*, Khulna University of Engineering & Technology, Khulna, Bangladesh. The above thesis work or any part of this work has not been submitted anywhere for the award of any degree or diploma.



07.10.2017

Signature of Supervisor



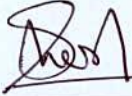

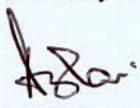
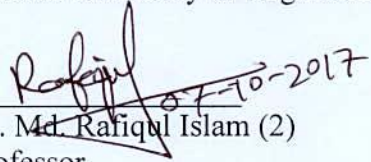
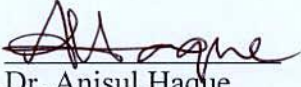
07.10.2017

Signature of Candidate

Approval

This is to certify that the thesis work submitted by *Ashrafal Hossain Howlader* entitled "*Vibrational Properties of Disordered Carbon Nanotube*" has been approved by the board of examiners for the partial fulfillment of the requirements for the degree of *Master of Science* in the Department of *Electrical and Electronic Engineering*, Khulna University of Engineering & Technology, Khulna, Bangladesh in October, 2017.

BOARD OF EXAMINERS

1.  07.10.2017
 Dr. Md. Sherajul Islam
 Associate Professor
 Department of Electrical and Electronic Engineering
 Khulna University of Engineering & Technology
 Chairman
 (Supervisor)
2. 
 Head of the Department
 Department of Electrical and Electronic Engineering
 Khulna University of Engineering & Technology
 Member
3. 
 Dr. Ashrafal Ghani Bhuiyan
 Professor
 Department of Electrical and Electronic Engineering
 Khulna University of Engineering & Technology
 Member
4. 
 Dr. Md. Rafiqul Islam (2)
 Professor
 Department of Electrical and Electronic Engineering
 Khulna University of Engineering & Technology
 Member
5. 
 Dr. Anisul Haque
 Professor
 Department of Electrical and Electronic Engineering
 East West University, Dhaka
 Member
 (External)

Acknowledgement

I would like to express my deepest gratitude to my supervisor and motivator **Dr. Md. Sherajul Islam**, Associate Professor, Department of Electrical and Electronic Engineering, Khulna University of Engineering & Technology, Khulna for his constant inspiration, valuable guidance and kind co-operation and finally helping me for providing necessary materials and sources during the entire period of my research work.

I am glad to thank all of my honorable teachers and supporting staffs in the department of Electrical and Electronic Engineering who have directly and indirectly helped me to do my job.

Last but not least, I would like to thank the authors of various research articles and books that are referred to.

Abstract

Carbon nanotube (CNT) is considered as an ideal candidate for next generation nanoelectronics owing to unusual thermal, electrical, optical and other physical properties. It provides the opportunity to understand one dimensional (1D) physics. Due to strong electron phonon coupling in carbon-based nanomaterials, lattice vibrations have a significant effect on the electron transport properties in CNT. From a realistic point of view, defects such as atomic vacancies, adatoms, isotopes and impurities are very common during the synthesis of CNTs. Even small concentration of vacancy changes the phonon properties of CNT significantly. Many studies on the vibrational properties of CNT have been performed. However, these works are limited on pristine CNT only. Here I have performed an in-depth theoretical analysis of the effect of vacancy defects and curvature on phonon properties of (10,0) zigzag semiconducting carbon nanotube (ZCNT) and (10,10) armchair metallic carbon nanotube (ACNT).

In the first part of this work, a simple model to calculate the vibrational eigenfrequencies and eigenvectors for 1D disordered systems is developed using the forced vibrational method, which is based on the mechanical resonance to extract the pure vibrational eigenmodes and suitable to treat very large and complex disorder physical system. This model is then used to study (10,0) ZCNT and (10,10) ACNT with different concentrations of atomic vacancies.

This dissertation reports some unique and interesting findings based on computational simulations on (10,0) and (10,10) CNTs both in low and high-frequency region. The correction of force constant parameters due to the curvature effect of CNTs lead to the Raman active E_{2g} mode phonon peaks are at 1576 cm^{-1} and 1581 cm^{-1} for (10,0) and (10,10) CNTs, respectively. A softening and shifting of the E_{2g} mode towards the low-frequency region are observed with the increasing of vacancies and curvature of CNTs. For vacancy concentrations of 10% or higher, the E_{2g} peak has been reduced into a shoulder or it has been completely disappeared. The other high symmetry point's peaks in the high-frequency region are also broadened and softened for both CNTs with the increase of defect density. Vacancy induces some new peaks at low-frequency region of phonon density of states.

Due to scattering by atomic vacancies, the phonon wave function becomes localized in the real space. To investigate phonon localization effect with vacancy type defects and curvature of

CNTs, the mode pattern and localization length for K point in-plane TO mode at Raman D-band frequency is calculated. Strong localization is observed with variation of vacancy concentration and curvature of CNTs. With increasing defect densities localization effect shows stronger confinement. The localization effect is stronger in (10,0) CNT than (10,10) CNT due to curvature effect.

These findings show the significant impact of vacancy defects on the phonon properties that strongly affect the electron transport properties of CNT-based nanodevices. These findings will also open a route towards better understanding the thermal conductivity, specific heat capacity, electron phonon interaction, resistivity and superconductivity in disordered CNT.

Contents

	PAGE
Title Page	i
Declaration	ii
Approval	iii
Acknowledgement	iv
Abstract	v
Contents	vii
List of Tables	ix
List of Figures	x
List of Acronyms	xiii
List of Symbols	xiv
CHAPTER I Introduction	1
1.1 Introduction	1
1.2 Motivation	5
1.3 Objectives	7
1.4 Synopsis of Dissertation	8
CHAPTER II Fundamentals of Single Wall Carbon Nanotube	9
2.1 Introduction	9
2.2 The sp^2 -hybridized Carbon Nanomaterials	9
2.3 Overview of SWCNT	12
2.4 Structure of SWCNT	13
2.5 Phonon Dispersion Relation and Phonon Density of States	17
2.5.1 Force Constant Model	17
2.6 Raman Spectroscopy	22
2.7 Vibrational Modes of SWCNT	23
2.7.1 Radial Breathing Mode	24
2.7.2 Tangential Mode	24
CHAPTER III Computational Details	26
3.1 Introduction	26
3.2 Normal Modes of Vibration	26
3.3 Forced Vibrational Method	27
3.4 Application of Force Vibrational Method to SWCNT	30

	3.5 Correction of Force Constants	33
	3.6 Periodic Boundary Condition	37
	3.7 Creation of Atomic Vacancies	38
CHAPTER IV	Results and Discussion	40
	4.1 Introduction	40
	4.2 Phonon Density of States of SWCNT	41
	4.3 Mode Pattern of SWCNT	45
	4.4 Localization Length of SWCNT	49
CHAPTER V	Summary and Outlook	51
	5.1 Conclusion	51
	5.2 Future Outlooks	52
	References	53
	List of Publications	60

LIST OF TABLES

Table No	Description	Page
2.1	Allotropes of sp^2 bonded carbon.	10
2.2	Parameters of SWCNT.	16
3.1	The angles (in degrees) between the central A type atom and different neighbors for (10,0) ZCNT and (10,10) ACNT (only x and y-axis will be interchanged).	32
3.2	The obtained nearest neighbor distances without curvature effect.	36
3.3	The obtained angles between A and B atoms.	36
3.4	The obtained force constants values taking into account the curvature effect.	36
3.5	Sample matrix element of (10,0) SWCNT of Figure 3.4. Here 1 and 0 represent the presence of atoms and absence of atoms respectively.	38

LIST OF FIGURES

Figure No	Description	Page
1.1	Some major applications of CNT in nanotechnology.	2
1.2	Global CNT market estimates and forecast, by application, 2012 - 2022 (Tons).	3
1.3	The annual number of published papers on CNT since their discovery until the end of 2010. Data were taken from www.scopus.com using carbon nanotube as keyword for article title.	3
2.1	The formation of sigma and pi bonds thorough the hybridization between two carbon atoms.	11
2.2	Honey comb lattice structure of carbon atoms.	11
2.3	Mono-layer 2D graphene. (b) Three layer graphene or graphite. (c) CNTs are rolled up cylinders of graphene. (d) Fullerenes (e.g. C ₆₀) are molecules consisting of wrapped graphene.	12
2.4	Rolling up of graphene sheet to form CNTs.	12
2.5	A graphic displaying a Chirality Map which shows the various types of SWCNTs that can be formed. The properties are governed by the way in which they are rolled as shown in the insets.	13
2.6	The unfolded SWCNT is shown along with the chiral and translational vector. The chiral vector OA or $C_h = na_1 + ma_2$ is defined on the honeycomb lattice by unit vectors a_1 and a_2 , and the chiral angle θ is defined with respect to the zigzag axis. Along the zigzag axis $\theta = 0^\circ$. Also there are shown the lattice vector $OB = T$ of the 1D tube unit cell, and the rotation angle ψ and the translation τ which constitute the basic symmetry operation $R = (\psi \tau)$. By rolling up a graphene sheet (a single layer of carbon atoms from a 3D graphite crystal) as a cylinder is formed. Shown here is a schematic theoretical model for a SWCNT with the tube axis OB normal to: The $\theta = 30^\circ$ direction (an "armchair" tube) and the $\theta = 0^\circ$ direction (a "zigzag" tube).	14
2.7	The Brillouin zone of a SWCNT is represented by the line segment WW' which is parallel to K_2 . The vectors K_1 and K_2 are	17

reciprocal lattice vectors corresponding to C_h and T , respectively.

- 2.8 (a) Neighbor atoms of graphene up to 4th nearest neighbors for A atom (similar results can be obtained for B atom). From the 1st to the 4th neighbor atoms, we plot solid circles. (b) Force constants between the A and B₁ atom on a planar graphene sheet. Here ϕ_r , ϕ_{ii} , and ϕ_{to} represent forces for the nearest neighbor atoms in the radial (bond stretching), in plane and out of plane tangential (bond bending) directions respectively. B₂ and B₃ are nearest neighbor equivalent to B₁, whose force constant tensors are obtained by appropriately rotating the tensor for A and B₁. 19
- 2.9 (a) The phonon dispersion curves, plotted along high symmetry directions, for a 2D SWCNT sheet. (b) The corresponding DOSs vs phonon energy for phonon modes in units of states/l Catom/cm⁻¹ × 10⁻². 20
- 2.10 (a) The calculated phonon dispersion relations of (10,10) ACNT. (b) PDOSs of (10,10) CNT. 21
- 2.11 Raman spectrum of SWCNT. 22
- 2.12 Raman scattering process for (a) the G peak (in plane transverse optic (iTO) plus in plane longitudinal optic (iLO) mode). (b) Phonon double resonance process for the D peak (intervalley scattering) and (c) the D' peak (intravalley scattering). 22
- 2.13 Raman-active normal mode eigenvectors and frequencies for a (10,10) CNT. The red arrows indicate the magnitude and direction of the appropriate carbon atom displacements, and the eigenvectors shown correspond to the seven most intense modes. The unit cell (blue atoms) is shown schematically in the upper right-hand corner. 25
- 3.1 A planar graphene sheet. The three shells of the nearest neighbors of the central A atom is shown by red circle. The directions of radial and tangential in-plane force constant tensors are labeled by ϕ_r and ϕ_{ii} respectively. The central A atom and the three B atoms from the first shell are labeled by 1, 2 and 3. In the similar way, second and third shells are labeled by the consecutive numbers. For (10,0) ZCNT and (10,10) ACNT only the x and y-axis will be interchanged. 31
- 3.2 (a) Brilluin zone of CNT with high symmetry points (b) Obtaining two dimensional graphene sheet from cylindrical CNT, chiral vector is along x-axis and translational vector along y-axis 34

	(c) (Top view of CNT) projection of B (filled circle) atom on xy-plane denoted as B' (unfilled circle) (d) (Side view of CNT) projection of B' (unfilled circle) on zx-plane denoted as B'' (unfilled circle).	
3.3	Periodic boundary conditions assume that there are no "ends." Point N is connected back to point 1 as if the structure were in the form of a ring making $(N+1)$ equivalent to 1.	37
3.4	(a) Unfolded (10,0) SWCNT (b) Application of PBC.	45
3.5	Example of disorder percolation network of honeycomb lattice.	39
4.1	Vacancy (about 30%) induced defective CNTs. (a) (10,0) semiconducting ZCNT and (b) (10,10) ACNT.	40
4.2	Raman active E_{2g} phonon mode direction at Γ point of Brillouin zone of (a) (10,0) CNT (b) (10,10) CNT (red arrows).	41
4.3	PDOSs of (a) (10,0) CNT (b) (10,10) CNT with variation of vacancy concentration over 0% - 30%.	43
4.4	Comparison of softening of Raman active E_{2g} mode of (10,0) and (10,10) CNTs with increasing defect densities.	44
4.5	Vibrational direction of D-band mode at K point of Brillouin zone of defective (a) (10,0) CNT (b) (10,10) CNT (red arrows).	45
4.6	Typical mode pattern of (a) pristine (b) 10% vacancy (c) 20% vacancy and (d) 30% vacancy induced (10,0) CNT. Each circle denotes an atom and the colors denote the displacement, which is linearly normalized. The vertical and horizontal axis are scaled in angstrom unit.	46
4.7	Typical mode pattern of (a) pristine (b) 10% vacancy (c) 20% vacancy and (d) 30% vacancy induced (10,10) CNT. Each circle denotes an atom and the colors denote the displacement, which is linearly normalized. The vertical and horizontal axis are scaled in angstrom unit.	47
4.8	Localization length as a function of defect density for both (10,0) and (10,10) CNTs.	49

List of Acronyms

CNT	Carbon Nanotube
SWCNT	Single Wall Carbon Nanotube
ACNT	Armchair Carbon Nanotube
ZCNT	Zigzag Carbon Nanotube
1D	One Dimension
2D	Two Dimension
DOS	Density of State
PDOS	Phonon Density of State
PBC	Periodic Boundary Condition
FCM	Force Constant Model
FVM	Force Vibrational Method
VHS	Van-Hove Singulaty
DR	Double Resonance
RBM	Radial Breathing Mode
HEM	High-Energy Mode

Nomenclature

C_h	Chiral vector
d_t	SWCNT diameter
θ	Chiral angle
n	Integer number
m	Integer number
a_1	Lattice vector
a_2	Lattice vector
t_1	Integer number
t_2	Integer number
L	Length of chiral vector
n_c	Number of carbon atom per unit cell of SWCNT
N	Number of hexagon per unit cell of SWCNT
d_R	Highest common divisor of (n, m)
K_1	Reciprocal lattice vector of SWCNT
K_2	Reciprocal lattice vector of SWCNT
b_1	Reciprocal lattice vectors
b_2	Reciprocal lattice vectors
M_l	Mass of l^{th} atom
$\phi_{ll'}$	Strength of the spring between the l^{th} and l'^{th} atoms
Q_λ	Amplitude of the normal mode λ
$e_l(\lambda)$	Polarization vector of mode λ
u_l	Scalar displacement of l^{th} atom
F_l	Periodic external force
F_0	Time independent constant amplitude
φ_l	A random number distributed uniformly from 0 to 2π
ω_m	Maximum frequency of the system
$g(\Omega)$	Phonon density of states
L_λ	Localization length of mode λ
r	radius

CHAPTER I

Introduction

1.1 Introduction

Carbon nanotube (CNT), an allotrope of carbon, is a unique one dimensional (1D) cylindrical nanomaterial with fascinating and attractive physical properties. CNT shows outstanding thermal, electronic and optical properties because of their nanosize which may vary with their length, diameter and chirality. According to measurements, an individual CNT has a room temperature thermal conductivity of about $3500 \text{ Wm}^{-1}\text{K}^{-1}$ with temperature stability up to 2800°C in vacuum and about 750°C in air [1]. The carrier mobility is found approximately $10,000 \text{ cm}^2\text{V}^{-1}\text{s}^{-1}$ and electric current density is about $4 \times 10^9 \text{ A/cm}^2$ [2]. The optical absorption coefficient of CNT is determined to be equal to $\sim 24 \times 10^4 \text{ cm}^{-1}$ [3]. The tensile strength is of range 30–45 GPa [4] and Young's modulus of 1.8 TPa [5], resulting from the sp^2 hybridized covalent bonds formed between the individual carbon atoms. It is highly flexible and has a large length to diameter ratio [6] with the value of order 10^5 - 10^{10} . CNT can be semiconducting or metallic depending on their chirality. Generally zigzag CNTs are semiconductor type and armchair CNTs are metal type. These intriguing physical properties proof CNT as one of the most promising multifunctional nanomaterials for numerous technological applications.

CNT provides exciting possibilities in implementing nanodevices for high-performance, high-power, and flexible nanoelectronics. CNT-based field effect transistors (FETs) operate much faster because of ballistic quantum transport of carrier originated from one dimensional (1D) quantum confinement [7]. The tunability of bandgap of semiconducting CNT is potentially useful in optics and photonics. With the narrow selectivity in the wavelength of emission and the ability of detection of light, as well as the possibility of fine tuning through the nanotube structure have made CNT a perfect material for light emitting diodes (LEDs) and photo detectors. CNTs possess a wide range of direct bandgaps matching with the solar spectrum as well as strong photo absorption capability ranges from infrared to ultraviolet, which make themselves an ideal photovoltaic material. Photovoltaic effect can be achieved

with ideal single CNT diodes and individual CNTs can form an ideal p-n junction diode [8]. Another benefit is that CNT-based transparent conductive films (TCFs) exhibit a high optical transparency in a broad spectral range [9] and can be used as conducting as well as transparent electrodes for hole collection in organic photovoltaic devices [10]. CNT is also a potential option for large scale interconnects (LSIs) [11]. CNTs are widely used in lithium ion batteries as electrodes [12]. CNT biosensors exhibit large changes in electrical impedance and optical properties in response to the surrounding environment [13]. CNTs can be used as electron guns due to its natural tunneling effect in miniature cathode ray tubes in high-brightness, low-energy, and low-weight field emission displays (FEDs) [14]. In Figure 1.1 some major applications of CNT are shown. Global CNT market estimates and forecast by application is demonstrated in Figure 1.2 and the annual number of published papers on CNT since their discovery until the end of 2010 is presented in Figure 1.3. Due to these versatile potentialities, CNTs have become an attractive and interesting research area in the field of nanotechnology and other emerging application fields.

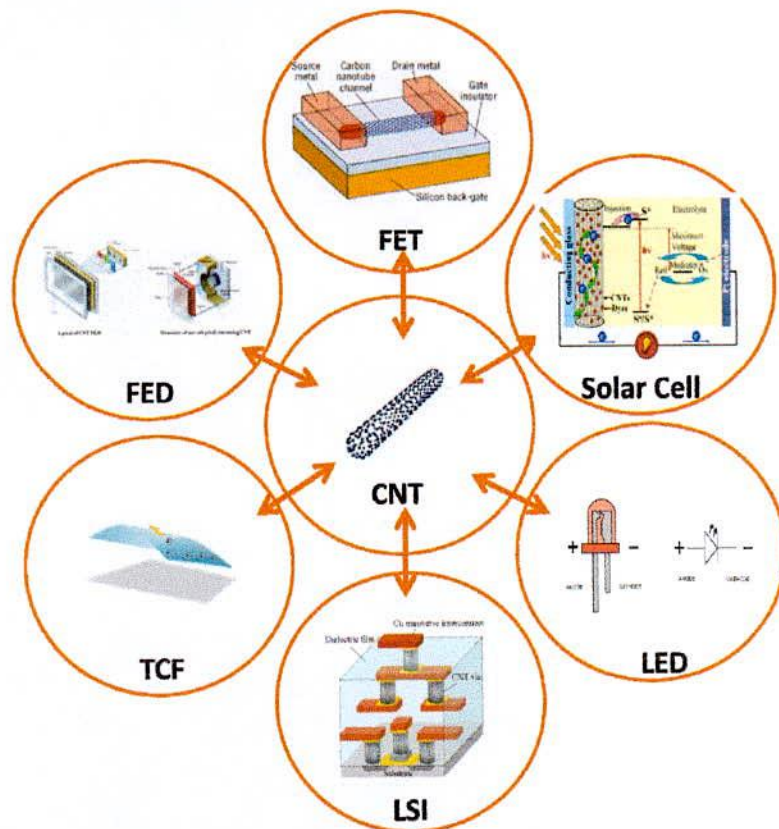


Figure 1.1: Some major applications of CNT in nanotechnology.

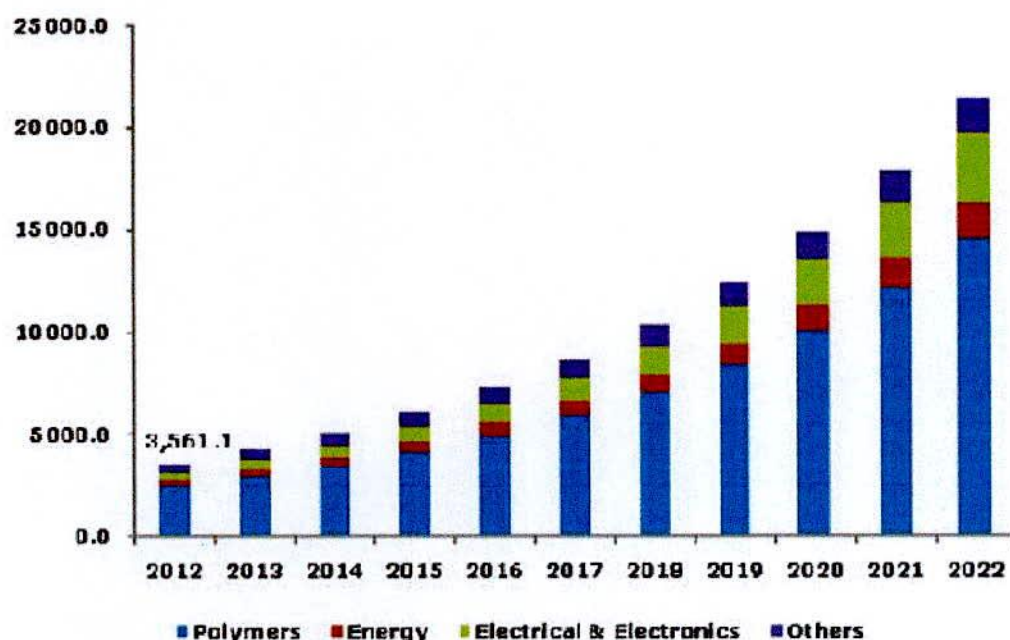


Figure 1.2: Global CNT market estimates and forecast, by application, 2012 - 2022 (Tons) [15].

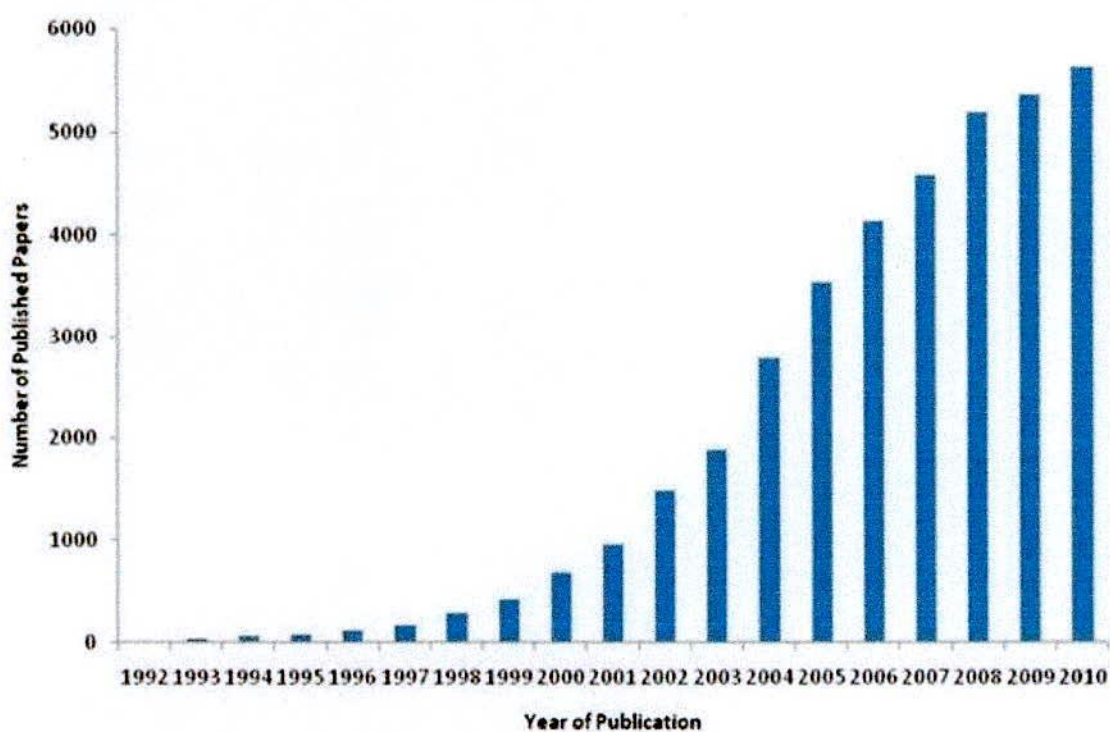


Figure 1.3: The annual number of published papers on CNT since their discovery until the end of 2010. Data were taken from www.scopus.com using carbon nanotube as keyword for article title [16].

CNTs have emerged in the field of nanotechnology because of their nanosize and unique physical properties. The fundamental characteristics of CNT comprise its vibrational properties and phonon spectrum, from which one can derive several physical properties. Phenomena such as charge [17-19], spin [20], heat transport [21-24], specific heat capacity [25], infrared and Raman spectra [26-28], electron phonon scattering [29-36] and its related effects such as resistivity [37] and superconductivity [38] can be understood, in most situations, only with a detailed knowledge of the phonon spectrum. Especially, many of these properties are determined by the low-energy phonon excitations. Furthermore, phonons play an important role in quasiparticle dynamics and electrical transport properties. Optical or electronic excitations can decay into vibrational excitations or can be scattered by phonons into different states. It has been suggested that the scattering between electrons and the optical phonon modes greatly affects the high-field ballistic transport properties in CNTs. In CNT, the electron phonon coupling strongly affects the phonon frequencies, giving rise to Kohn anomalies and possible soft modes or Peierls distortions [31,39,40]. Moreover, there is currently a debate on the vibrational origins of superconductivity in CNT [38] and it is the subtle interplay between phonons and electrons that gives rise to this phenomena. In technological applications such as CNT-based electronic devices, thermal properties are of central importance for understanding and controlling heat dissipation and self-heating effects. Efficient thermal management is required for ensuring the performance and stability of these devices. The quantitative understanding and characterization of this effect and other related phenomena require a detailed knowledge of the vibration and phonon properties of CNT.

A realistic CNT is not defect-free, and it unavoidably contains many kinds of structural defects and disorders, which can be generated during the growth. CNT obviously cannot contain higher dimensional defects like line and screw dislocations. The common structural defects existing in CNT are atomic vacancies. There can be also impurities and adatoms present in CNT. The vacancy defects found in graphene are more complicated in CNTs because of circumferential and curvature induced strain. For a given CNT containing atomic vacancies, the atomic structure around the defect is quite different from that of the perfect portion. When vacancy disorders occur in CNT, the dangling bonds are created at the vacancy sites and destroy the original local σ -like hybridization around the vacancy by breaking the local symmetric structure of a perfect CNT [41]. It is natural to expect that even small

concentrations of vacancy defects in CNT nanostructures may lead to specific shifts, broadenings and additional characteristic singularities in the phonon and electron densities of states. The loss of thermal conductivity, the increase in electrical resistance and the change in optical activity can be attributed to atomic vacancy defects. Such phenomena are certainly crucial to the newly emerging field of nanotechnology, in which low dimensional nanoscaled materials are synthesized, characterized, and integrated into applications. Therefore, studying the vacancy defects effect on the vibrational properties of CNT is one of the fundamental issues for its potential applications.

1.2 Motivation

The synthesis of single wall carbon nanotube (SWCNT) has opened a new era in the field of nanoelectronics. Due to a strong electron phonon coupling in carbon based low dimensional materials, lattice vibrations have a significant effect on the electron transport properties of CNT-based nanoelectronic devices. From a realistic point of view, during the synthesis of CNT, random atomic vacancies, adatoms, isotopes and impurities are created. Among intrinsic defects, atomic vacancies are the most common, existing even in nearly defect free CNT. This type of inherent vacancy induced atomic disorder undoubtedly would influence vibrational properties of CNT, because in sp^2 bonded carbon materials, the behavior of the phonons, just like the electrons, depends on the atomic structure. Even a small amount of vacancy type defects in CNT like quasi 1D structure, may alter the vibrational properties significantly and thus change their electrical transport properties.

In sp^2 hybridized carbon-carbon bonded family materials the phonon wave function is considered as delocalized in the crystal system. An atomic vacancy disorder in a crystalline system may shift the vibrational modes outside of the allowed frequency range of the perfect crystal [42,43]. These are called localized vibrational modes because the mode energy is spatially concentrated at the defect sites. When the vibrational modes become localized, the mean free path of the phonon becomes finite and proportional to the square of the localization length. These phonons with finite lifetime and finite localization length are the main contributors to the natural line width of the Raman spectra for a particular crystalline system. Phonons confined in a 1D system should follow a single trajectory and cannot avoid a scattering center nor scatter into nearby momentum states due to vacancy defects. These

localized phonons should have significant effects on electron transport of CNT. Especially the high-frequency optic phonons are more strongly coupled with electrons than to low-frequency acoustic phonons. CNTs, with their uniquely simple crystal structures and chirality dependent vibrational and electronic states, provide a 1D playground for studying the dynamics and interactions of phonons and electrons. Thus the investigation of the defect induced phonon properties of CNT is of fundamental importance for understanding the electron transport in CNT-based molecular electronics.

The crystalline disorder shows some special phonon properties in sp^2 hybridized carbon systems. For example, strong D-band feature is observed in the Raman spectra which is generally inactive in perfect CNT and phonons are the main source of Raman spectra in the literature [44]. The defect induced resonant Raman scattering occurs due to the breakdown of the crystalline symmetry in CNT by introducing vacancy disorder into the crystal lattice system through the activation of phonons at interior K points on the Brillouin zone boundary. To understand these phenomena, the detail knowledge of phonon properties of disordered CNTs is indispensable.

Many significant contributions have been devoted to the phonon properties of CNT based on theoretical approaches, including tight binding method [45], first-principle calculations [30,46,47] and force constant model (FCM) [48] in the previous few decades. Yu et al. [45] applied tight binding method to investigate phonon properties of CNT with different chiralities. They were able to capture part of the curvature induced strain effect of CNT on its phonon density of states (PDOSs) through the geometry dependence of its matrix elements, even though their absolute value depend on the intrinsic structure of graphite. In their pioneering work, Sánchez-Portal et al. [46] used ab initio density functional theory based first principle calculation, which combined pseudopotential with the representation of wave functions by linear combination of atomic orbitals to calculate the force constants of CNT. Because of the incompleteness of their basis set, the general accuracy of the phonon property was not quite good. The second group of work using first principle calculation was done by Dubay et al. [30] on armchair (ACNT) and zigzag carbon nanotube (ZCNT). The calculations are performed using a plane wave basis set and density functional theory. The improvement on the high-energy phonon property was obvious. But clear error happened on the low-energy region where as some inconsistency is found for the intermediate frequency region. Ye et al.

[47] made a systematic first principle ab initio study on the phonon dispersions for a series of achiral CNT's by the supercell approach. The calculations were extended to some very small CNTs to reflect more clearly the curvature effect. They obtained good accuracy on the full frequency range of PDOS of CNT. First principle calculations are superior in terms of their predictive capabilities on PDOS of CNT, although sometimes the calculated results give imaginary frequencies for the acoustic modes of CNTs. The FCM by Saito et al. [48] provided PDOS with force constants corrected considering curvature effect of CNT by applying periodic boundary condition (PBC) to the circumferential direction of the CNT. All of the theoretical experiment discussed above focused mainly on the pristine CNTs only. However, as far as it is known, the phonon properties of vacancy induced CNTs have been remained unexplored. A detailed analysis of this problem in realistic systems at the atomic scale is still lacking. Again, if atomic vacancies are present in a crystal system, the symmetry of elemental topological arrangements of the crystal system breaks down, which generate more complex lattice structure. Therefore, the dynamical matrix method requires huge computational resources. This long computational time and convergence problems with the dynamical matrix calculations, limit the systems of interest into few number of atoms. Moreover, an in-depth understanding of the phonon properties of CNT is hindered by an inability to deal with a large number of carbon atoms. That is why, a larger scale model is essential for complete understanding of vibrational properties of vacancy defective atomic structures of CNT. It is thus crucial to build a realistic model to have an intense observation on the phonon properties of the vacancy disordered CNT.

1.3 Objectives

The purpose of this dissertation is to go through systematically the details of the various vacancy concentration effects on the vibrational properties of (10,0) semiconductor ZCNT and (10,10) metallic ACNT. The forced vibrational method (FVM) introduced by Williams and Marris [49] has been employed for developing a well defined quantitative model to estimate the vibrational properties of disordered (10,0) and (10,10) SWCNT systems. This method is based on the principle that a linear and large disordered mechanical system when driven by a periodic external force of certain frequency will respond with large amplitudes in those eigenmodes close to this frequency. This technique has the following advantages:

- I. One can apply this algorithm to a very large, complex as well as disordered system. This algorithm requires a memory space of order N .
- II. It is possible to calculate quite accurately the density of states (DOSs) in both low-frequency and high-frequency regime.
- III. The magnitude of the DOS at any frequency can be obtained by sweeping the resonant frequency.

In the course of this dissertation, the following objectives were achieved:

1. Develop a reliable model based on the FVM technique to determine the vibrational properties of vacancy disordered (10,0) and (10,10) SWCNTs.
2. Report the effects of vacancy-type defects on the phonon properties of SWCNTs for the first time.
3. Report the effects of curvature on the phonon properties of SWCNTs.
4. To quantify the localization properties due to vacancy type defects and curvature is another important objective.

1.4 Synopsis of Dissertation

CHAPTER II gives an overview of the basic concepts for SWCNT in order to establish a basis for discussing the obtained results in the later chapters. After introducing the different types of carbon nanostructures, emphasis is laid on the fundamentals of SWCNT, vibrational properties of SWCNT and their influences on the Raman spectra.

CHAPTER III introduces the used computational technique, which allows calculating the very large and complex disordered systems.

CHAPTER IV presents the vibrational properties of vacancy disordered (10,0) ZCNT and (10,10) ACNT with the aid of the forced vibrational method in detail. This is complemented by the phonon density of states, typical mode patterns and phonon localization length of vacancy type disordered SWCNT.

CHAPTER V provides a summary of the most relevant results, combined with an outlook on possible future research directions.

CHAPTER II

Fundamentals of Single Wall Carbon Nanotube

2.1 Introduction

This chapter is intended to provide an introduction and overview of the fundamental concepts of SWCNT. The fundamentals and classification of SWCNT, vibrational properties and Raman spectra of SWCNT have been discussed that will be useful to understand the results in the later chapters.

2.2 The sp^2 -hybridized Carbon Nanomaterials

Carbon is the 15th most abundant element in the earth's crust, and the fourth most abundant element in the universe by mass. Carbon is a group IV element with symbol C and atomic number 6. It is nonmetallic and tetravalent making four electrons available to form covalent chemical bonds. Carbon is the sixth element, with a ground state electron configuration of $1s^2 2s^2 2p^2$, of which the four outer electrons are valence electrons. Its first four ionization energies, 1086.5, 2352.6, 4620.5 and 6222.7 kJ/mol is much higher than those of the heavier group 14 elements. The electro negativity of carbon is 2.5, significantly higher than the heavier group 14 elements (1.8–1.9), but close to most of the nearby nonmetals as well as some of the second and third row transition metals. Carbon's covalent radii are normally taken as 77.2 pm (C–C), 66.7 pm (C=C) and 60.3 pm (C≡C), although these may vary depending on coordination number and what the carbon is bonded to. In general, covalent radius decreases with lower coordination number and higher bond order [50]. Three isotopes occur naturally, ^{12}C and ^{13}C being stable, while ^{14}C is a radioactive isotope, decaying with a half-life of about 5,730 years [51]. The atoms of carbon can bond together in different ways, termed allotropes of carbon. The best known are graphite, diamond and amorphous carbon. Carbon is capable of forming many more allotropes due to its valence electron configuration such as buckminsterfullerene, graphene, CNTs, nanobuds and nanoribbons. The physical properties of carbon vary widely with the allotropic form. For example, graphite is opaque and black while diamond is highly transparent. Graphite is soft enough to form a streak on while diamond is

the hardest naturally occurring material known. Graphite is a good electrical conductor while diamond has a low electrical conductivity. Under normal conditions diamond, CNT and graphene have the highest thermal conductivities of all known materials. All carbon allotropes are solids under normal conditions, with graphite being the most thermodynamically stable form. They are chemically resistant and require high temperature to react even with oxygen.

Generally, four valence electrons in carbon tend to interact with each other to produce the various types of allotrope. When carbon atoms come together to form a crystal, one of the 2s electrons is excited to the 2p_z orbital gaining energy from the neighboring nuclei, which has net effect of lowering the overall energy of the system. Interactions or bonding subsequently follow between the 2s and 2p orbitals of neighboring carbon atoms. These interactions or mixing of atomic orbitals is commonly called the hybridization, and the new orbitals that are formed are referred to as hybrid orbitals. Figures 2.1 and 2.2 illustrate the formation of the covalent bond through the hybridization between the carbon atoms in carbon honeycomb lattice. The sp² hybridization of the singly occupied 2s orbital and two 2p orbitals (e.g. p_x and p_y) leads to a trigonal planar structure, with an in-plane bond between two neighboring carbon atoms. Additionally, the singly occupied p_z orbital of a carbon atom which is perpendicular to the planar structure bonds with the p_z orbitals of neighboring carbon atoms leading to the formation of a delocalized band, which is half-filled [52]. The existence of multiple flavors of hybridization in carbon is what leads to the different allotropes shown in Table 2.1. Graphene, a layer of carbon atoms arranged into a 2D hexagonal lattice, is a single layer of graphite (see Figures 2.3(a) and 2.3(b)) [53]. CNTs represent rolled-up cylinders of graphene (see Figure 2.3(c)) [54-56]. Fullerene [57] molecules (e.g. C₆₀) are obtained by wrapping graphene, combined with the introduction of pentagons into the hexagonal lattice (see Figure 2.3(d)).

Table 2.1: Allotropes of sp² bonded carbon [58].

Dimension	0D	1D	2D	3D
Allotrope	C ₆₀ bucky ball	CNT	Graphene	Graphite
Structure	Spherical	Cylindrical	Planar	Stacked planar
Hybridization	sp ²	sp ²	sp ²	sp ²
Electronic properties	Semiconductor	Metal or Semiconductor	Semi-metal	Metal

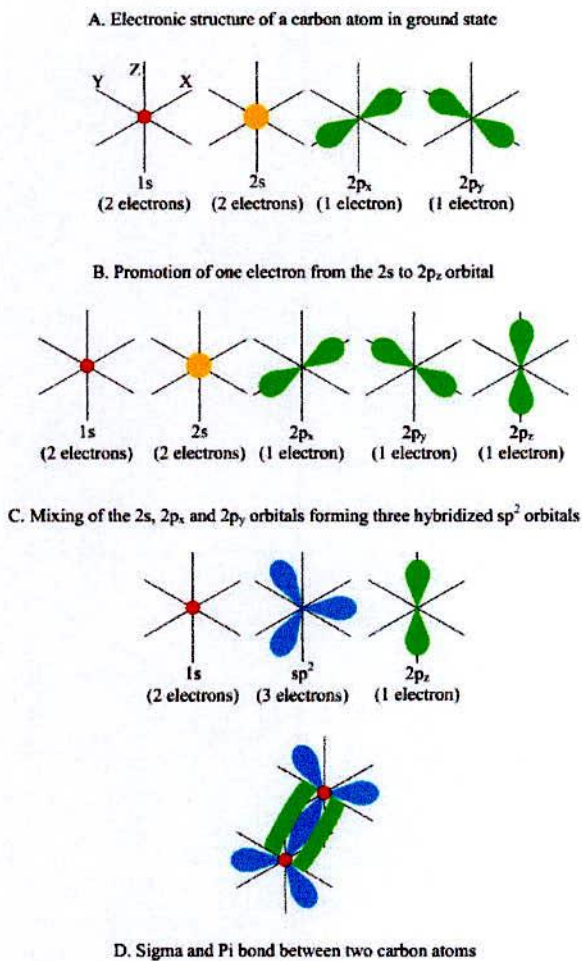


Figure 2.1: The formation of sigma and pi bonds through the hybridization between two carbon atoms [58].

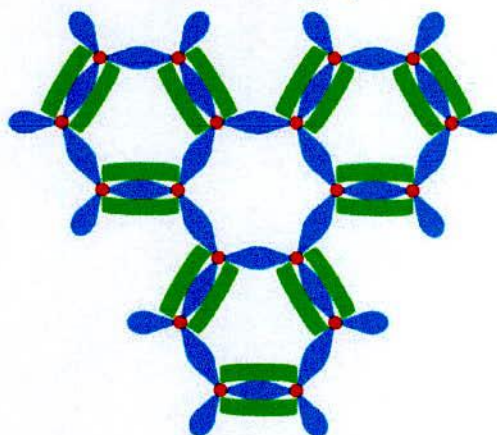


Figure 2.2: Honey comb lattice structure of carbon atoms [58].

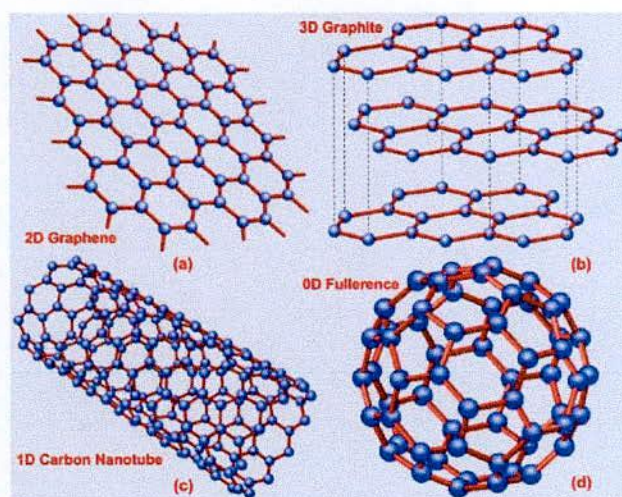


Figure 2.3: (a) Mono-layer 2D graphene. (b) Three layer graphene or graphite. (c) CNTs are rolled up cylinders of graphene. (d) Fullerenes (e.g. C_{60}) are molecules consisting of wrapped graphene [59].

2.3 Overview of SWCNT

The CNTs are synthesized in a large variety of structures. Some of them consist of a single cylindrical graphene layer, so called SWCNT as shown in Figure. 2.4. Others comprise a number of coaxial layers, so called multiwall carbon nanotubes. An interesting and essential fact about the structure of a CNT is the orientation of the six-membered carbon ring (hereafter called a hexagon) in the honeycomb lattice relative to the axis of the nanotube as shown in Figure 2.4. From this figure, it can be seen that the direction of the six-membered ring in the honeycomb lattice can be taken almost arbitrarily, without any distortion of the hexagons except for the distortion due to the curvature of the carbon nanotube. This fact provides many possible structures for carbon nanotubes, even though the basic shape of the CNT wall is a cylinder.

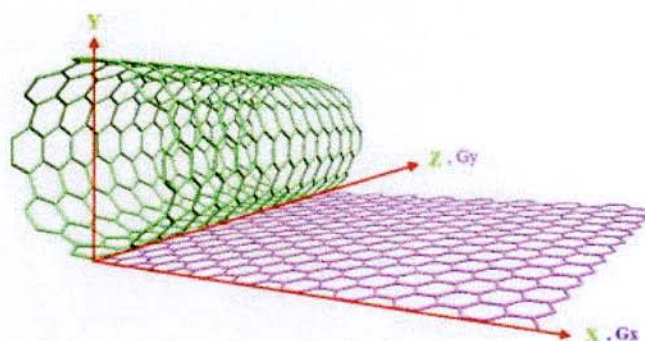


Figure 2.4: Rolling up of graphene sheet to form CNTs [60].

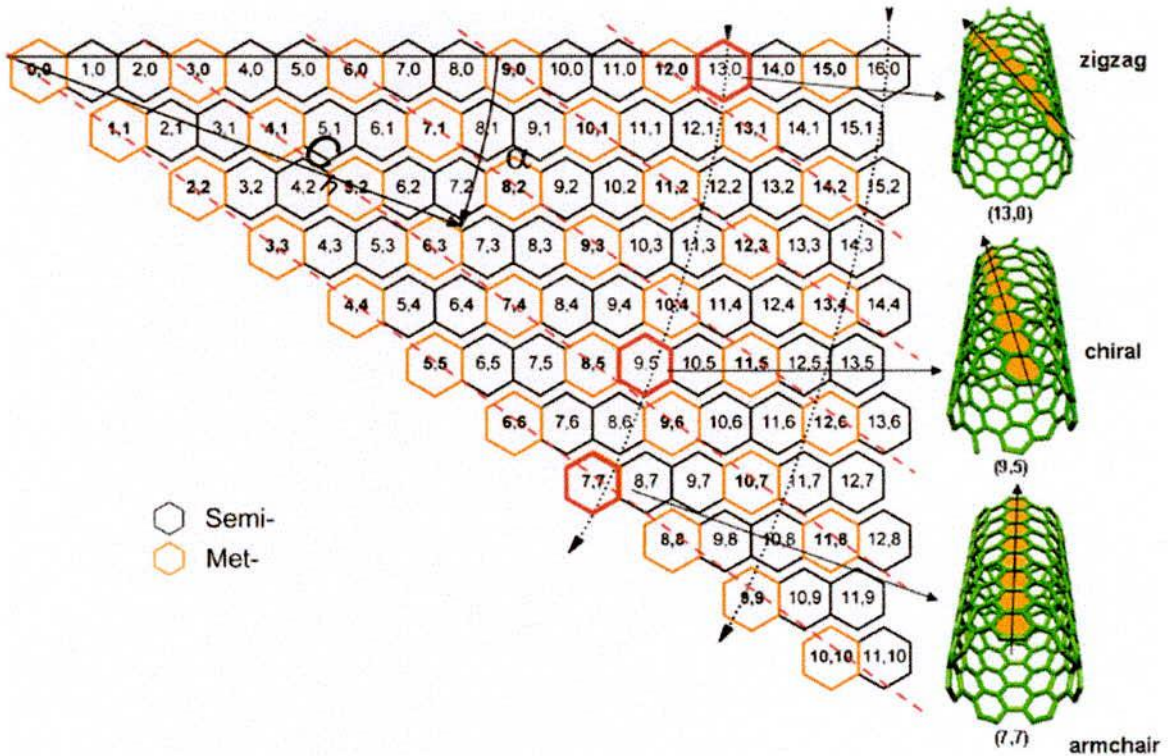


Figure 2.5: A graphic displaying a Chirality Map which shows the various types of SWCNTs that can be formed. The properties are governed by the way in which they are rolled as shown in the insets [61].

The primary symmetry classification of a carbon nanotube is as either being achiral (symmorphic) or chiral (non-symmorphic). An achiral carbon nanotube is defined by a CNT whose mirror image has an identical structure to the original one. There are only two cases of achiral nanotubes: ACNTs (n,n) and ZCNTs $(n,0)$ as are shown from the Chirality Map of CNTs in Figure 2.5. The names of armchair and zigzag arise from the shape of the cross-sectional ring at the edge of the nanotubes. Chiral nanotubes exhibit a spiral symmetry whose mirror image cannot be superposed on to the original one. We have thus a variety of geometries in CNTs which can change diameter and chirality [62].

2.4 Structure of SWCNT

It is convenient to specify a general CNT in terms of the tube diameter d_t , and the chiral angle θ , which are shown in Figure 2.6. The chiral vector C_h is defined in terms of the integers (n,m) and the basis vectors \mathbf{a}_1 and \mathbf{a}_2 of the honeycomb lattice,

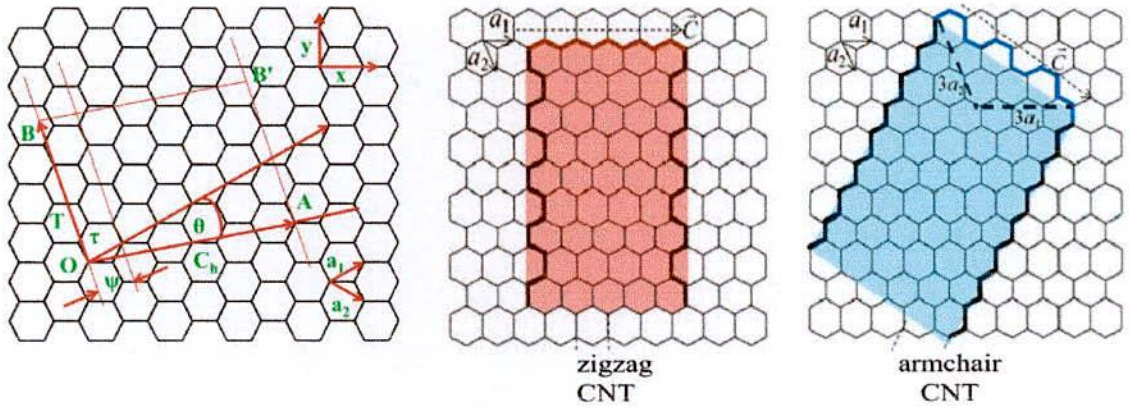


Figure 2.6: The unfolded SWCNT is shown along with the chiral and translational vector. The chiral vector OA or $C_h = na_1 + ma_2$ is defined on the honeycomb lattice by unit vectors a_1 and a_2 , and the chiral angle θ is defined with respect to the zigzag axis. Along the zigzag axis $\theta = 0^\circ$. Also there are shown the lattice vector $OB = T$ of the 1D tube unit cell, and the rotation angle ψ and the translation τ which constitute the basic symmetry operation $R = (\psi | \tau)$. By rolling up a graphene sheet (a single layer of carbon atoms from a 3D graphite crystal) as a cylinder is formed. Shown here is a schematic theoretical model for a SWCNT with the tube axis OB normal to: The $\theta = 30^\circ$ direction (an “armchair” tube) and the $\theta = 0^\circ$ direction (a “zigzag” tube).

which are also defined in terms of rectangular coordinates. The integers (n, m) uniquely determine d_t and θ . The length L of the chiral vector C_h (see table 2.2) is directly related to the tube diameter d_t . The chiral angle θ between the C_h direction and the zigzag direction of the honeycomb lattice $(n, 0)$ (see Figure 2.6) is related to the integers (n, m) in Table 2.2.

The unit cell of the CNT is shown in Figure 2.6 with the rectangle bounded by the vectors C_h and T , where T is the 1D translation vector of the nanotube. The vector T is normal to C_h and extends from the origin to the first lattice point B in the honeycomb lattice. It is convenient to express T in terms of the integers (t_1, t_2) , where it is seen that the length of T is $\sqrt{3}L/d_R$ and d_R is either equal to the highest common divisor of (n, m) , denoted by d , or to $3d$, depending on whether $n-m = 3d_r$, r being an integer, or not (see Table 2.2). The number of carbon atoms per unit cell n_c , of the 1D tube is $2N$, as given in Table 2.2, each hexagon (or unit cell) of the honeycomb lattice containing two carbon atoms [63]. The chiral vector C_h can be derived as follows :

$$\begin{aligned} \mathbf{C}_h &= n\mathbf{a}_1 + m\mathbf{a}_2 \\ &= na \left(\frac{\sqrt{3}}{2} \mathbf{x} + \frac{1}{2} \mathbf{y} \right) + ma \left(\frac{\sqrt{3}}{2} \mathbf{x} - \frac{1}{2} \mathbf{y} \right) = \frac{\sqrt{3}}{2} a(n+m)\mathbf{x} + \frac{1}{2} a(n-m)\mathbf{y} \end{aligned} \quad 2.1$$

$$L = |\mathbf{C}_h| = a \sqrt{\frac{3}{4}(n+m)^2 + \frac{1}{4}(n-m)^2} = a\sqrt{n^2 + nm + m^2} \quad 2.2$$

The translation vector can be derived as \mathbf{T} can be derived as follows:

$$\begin{aligned} \mathbf{T} &= t_1\mathbf{a}_1 - t_2\mathbf{a}_2 \\ &= \frac{(2m+n)}{d_R}\mathbf{a}_1 - \frac{(2n+m)}{d_R}\mathbf{a}_2 \\ &= \frac{(2m+n)}{d_R} \left(\frac{\sqrt{3}}{2} \mathbf{x} + \frac{1}{2} \mathbf{y} \right) a - \frac{(2n+m)}{d_R} \left(\frac{\sqrt{3}}{2} \mathbf{x} - \frac{1}{2} \mathbf{y} \right) a = \frac{\sqrt{3}a}{2d_R}(m-n)\mathbf{x} + \frac{3a}{2d_R}(n+m)\mathbf{y} \end{aligned} \quad 2.3$$

$$|\mathbf{T}| = \frac{\sqrt{3}a}{2d_R} \sqrt{(m-n)^2 + 3(n+m)^2} = \frac{\sqrt{3}a}{d_R} \sqrt{n^2 + nm + m^2} = \frac{\sqrt{3}aL}{d_R} \quad 2.4$$

Since there are $2N$ carbon atoms in this unit cell, we will have N pairs of bonding π and anti-bonding π^* electronic energy bands. Similarly the phonon dispersion relations will consist of $6N$ branches resulting from a vector displacement of each carbon atom in the unit cell.

Expressions for the reciprocal lattice vectors \mathbf{K}_2 along the nanotube axis and \mathbf{K}_1 in the circumferential direction are obtained from the relation $\mathbf{R}_i \cdot \mathbf{K}_j = 2\pi\delta_{ij}$, where \mathbf{R}_i and \mathbf{K}_j are, respectively, the lattice vectors in real and reciprocal space. Since nanotubes are 1D material, only \mathbf{K}_2 is a reciprocal lattice vector. \mathbf{K}_1 gives discrete k values in the direction of \mathbf{C}_h . Then we get:

$$\mathbf{C}_h \cdot \mathbf{K}_1 = 2\pi \quad 2.5$$

$$\mathbf{C}_h \cdot \mathbf{K}_2 = 0 \quad 2.6$$

$$\mathbf{T} \cdot \mathbf{K}_1 = 0 \quad 2.7$$

$$\mathbf{T} \cdot \mathbf{K}_2 = 2\pi \quad 2.8$$

We get expressions for \mathbf{K}_1 and \mathbf{K}_2 :

$$\mathbf{K}_1 = \frac{1}{N} (-t_2\mathbf{b}_1 + t_1\mathbf{b}_2) \quad 2.9$$

$$\mathbf{K}_2 = \frac{1}{N} (m\mathbf{b}_1 - n\mathbf{b}_2) \quad 2.10$$

where \mathbf{b}_1 and \mathbf{b}_2 are the reciprocal basis vectors of two dimensional graphene plane. In Figure 2.7, we show the reciprocal lattice vectors, \mathbf{K}_1 and \mathbf{K}_2 . The first Brillouin zone of this quasi 1D unique material is the line segment WW' . Since $N\mathbf{K}_1 = -t_2\mathbf{b}_1 + t_1\mathbf{b}_2$ corresponds to a reciprocal lattice vector of 2D graphene plane, two wave vectors which differ by $N\mathbf{K}_1$ are equivalent.

Table 2.2 : Parameters of SWCNT [63]

Symbol	Name	Formula	Value
a_{c-c}	carbon-carbon distance		1.42 Å (graphite)
a	length of unit vector	$\sqrt{3} a_{c-c}$	2.46 Å
$\mathbf{a}_1, \mathbf{a}_2$	unit vectors	$\left(\frac{\sqrt{3}}{2}, \frac{1}{2}\right) a, \left(\frac{\sqrt{3}}{2}, -\frac{1}{2}\right) a$	in (x,y) coordinates
$\mathbf{b}_1, \mathbf{b}_2$	reciprocal lattice vectors	$\left(\frac{1}{\sqrt{3}}, 1\right) \frac{2\pi}{a}, \left(\frac{1}{\sqrt{3}}, -1\right) \frac{2\pi}{a}$	in (x,y) coordinates
\mathbf{C}_h	chiral vector	$\mathbf{C}_h = n\mathbf{a}_1 + m\mathbf{a}_2 \equiv (n, m)$	n, m : integers
L	circumference of nanotube	$L = \mathbf{C}_h = a\sqrt{n^2 + nm + m^2}$	$0 \leq m \leq n$
d_t	diameter of nanotube	$d_t = \frac{L}{\pi} = \frac{\sqrt{n^2 + nm + m^2}}{\pi} a$	
θ	chiral angle	$\sin\theta = \frac{\sqrt{3}m}{2\sqrt{n^2 + m^2 + nm}}$ $\cos\theta = \frac{2n + m}{2\sqrt{n^2 + nm + m^2}}$ $\tan\theta = \frac{\sqrt{3}m}{2n + m}$	$0 \leq \theta \leq 30^\circ$
d	the highest common divisor of (n,m)		
d_R	the highest common divisor of (2n+m, 2m+n)	$d_R = d$ if $n - m$ not a multiple of 3d $= 3d$ if $n - m$ a multiple of 3d	
\mathbf{T}	translational vector of 1D unit cell	$\mathbf{T} = t_1\mathbf{a}_1 + t_2\mathbf{a}_2 \equiv (t_1, t_2)$ $t_1 = \frac{2m + n}{d_R}$ $t_2 = -\frac{d_R}{2n + m}$	t_1, t_2 : integer
T	length of \mathbf{T}	$ \mathbf{T} = \frac{\sqrt{3}L}{d_R}$	
N	number of hexagon per 1D unit cell	$N = \frac{2(n^2 + m^2 + nm)}{d_R}$	$2N \equiv \frac{n_c}{\text{unit cell}}$
\mathbf{R}	symmetry vector [†]	$\mathbf{R} = p\mathbf{a}_1 + q\mathbf{a}_2 \equiv (p, q)$ $d = mp = nq, 0 \leq p \leq n/d, 0 \leq q \leq m/d$	p, q : integers [†]
M	number of 2π revolutions	$M = [(2n + m)p + (2m + n)q]/d_R$ $NR = M\mathbf{C}_h + d\mathbf{T}$	M : integer
R	basic symmetry operations [‡]	$ \mathbf{R} = (\psi \tau)$	
ψ	rotation operation	$\psi = 2\pi \frac{M}{N}, \left(\kappa = \frac{\psi L}{2\pi}\right)$	ψ : radians
τ	translation operation	$\tau = \frac{dT}{N}$	τ, κ : length

[†](p,q) are uniquely determined by $d=mp-nq$, subject to conditions stated in table, except for zigzag tubes for which $\mathbf{C}_h = (n,0)$, and we define $p=1, q=-1$, which gives $M=1$.

[‡] \mathbf{R} and $|\mathbf{R}|$ refer to the same symmetry operation.

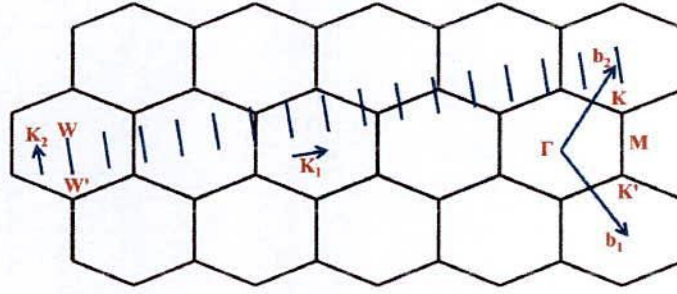


Figure 2.7: The Brillouin zone of a SWCNT is represented by the line segment WW' which is parallel to \mathbf{K}_2 . The vectors \mathbf{K}_1 and \mathbf{K}_2 are reciprocal lattice vectors corresponding to \mathbf{C}_h and \mathbf{T} , respectively.

Since t_1 and t_2 do not have a common divisor except for unity, none of the $N-1$ vectors $\mu\mathbf{K}_1$ (where, $\mu = 1, \dots, N-1$) are reciprocal lattice vectors of two dimensional graphene plane. Thus the N wave vectors $\mu\mathbf{K}_1$ ($\mu = 0, \dots, N-1$) give rise to N discrete k vectors, as indicated by the N parallel line segments in Figure 2.7, which arise from the quantized wave vectors associated with the PBC on \mathbf{C}_h . The length of all the parallel lines in Figure 2.7 is $2\pi/T$ which is the length of the 1D first Brillouin zone. For the N discrete values of the \mathbf{k} vectors, N 1D energy bands will appear. Because of the translational symmetry of \mathbf{T} , we have continuous wave vectors in the direction of \mathbf{K}_2 for a CNT of infinite length. However, for a nanotube of finite length L_t , the spacing between wave vectors is $2\pi/L_t$ [63].

2.5 Phonon Dispersion Relation and Phonon Density States

The phonon dispersion relations of carbon nanotubes can be understood by zone folding the phonon dispersion curves for a single 2D graphene sheet. The vibrational properties of CNT can be calculated within a tight binding method [45], first principle calculations [30, 46, 47] or force constant model [48]. In this work we concentrate on the well established fourth nearest neighbors force constant model by Jishi et al. [64]. It was developed and optimized for graphene and subsequently also adapted to CNT by Saito et al. [48].

2.5.1 Force Constant Model

In the FCM, interactions including as many nearest neighbors in the graphene sheet can be considered in order to improve the agreement with experiment. In general, the equations of

motion for the displacement of the i^{th} atom measured from the equivalent position, $u_i = (x_i, y_i, z_i)$ for N atoms in the unit cell is given by:

$$M_i \ddot{u}_i = \sum_j K^{(i,j)} (u_j - u_i), \quad (i = 1, \dots, N) \quad 2.11$$

Where M_i is the mass of the i^{th} atom and $K^{(i,j)}$ represents the 3×3 force constant tensor between the i^{th} and the j^{th} atoms. The sum over j in Equation 2.11 is normally taken over only a few neighbor distances relative to its site, which for a 2D graphene sheet has been carried out up to fourth nearest neighbor interactions. In a periodic system we can perform a Fourier transform of the displacement of the i^{th} atom with the wave number k' to obtain the normal mode displacement $u_k^{(i)}$.

$$u_i = \frac{1}{\sqrt{N_\Omega}} \sum_{q'} e^{-i(q' \cdot R_i - \omega t)} u_{q'}^{(i)} \quad 2.12$$

or

$$u_q^{(i)} = \frac{1}{\sqrt{N_\Omega}} \sum_{R_i} e^{i(q \cdot R_i - \omega t)} u_i \quad 2.13$$

in which the sum is taken over all (N_Ω) wave vectors q' in the first Brillouin zone and R_i denotes the atomic position of the i^{th} atom in the crystal. When we assume the same eigenfrequencies ω for all u_i , that is $\ddot{u}_i = -\omega^2 u_i$, then Equation 2.11 can formally written by defining a $3N \times 3N$ dynamical matrix $D(q)$.

$$D(q) u_q = 0 \quad 2.14$$

To obtain the eigenvalues $\omega^2(q)$ for $D(q)$ and nontrivial eigenvectors $u_q \neq 0$, we solve the secular equation $\det D(q) = 0$ for a given q vector. It is convenient to divide the dynamical matrix $D(q)$ into small 3×3 matrices $D^{ij}(q)$, ($i, j = 1, \dots, N$), where we denote $D(q)$ by $\{D^{(ij)}(q)\}$, and from Eq. 2.14 it follows that $D^{(ij)}(q)$ is expressed as:

$$D^{(ij)}(q) = \left(\sum_{j''} K^{(ij'')} - M_i \omega^2(q) I \right) \delta_{ij} - \sum_{j'} K^{(ij')} e^{iq \cdot \Delta R_{ij'}} \quad 2.15$$

in which I is a 3×3 unit matrix and $\Delta R_{ij} = R_i - R_j$ is the relative coordinates of the i^{th} atom with respect to the j^{th} atom. The vibration of the i^{th} atom is coupled to that of the j^{th} atom through the K^{ij} force constant tensor.

In planar graphene sheet, since there are two distinct carbon atoms A and B in the unit cell, we must consider six coordinates u_k (or 6 degrees of freedom) in Equation 2.15. The secular equation to be solved is thus a 6×6 dynamical matrix D . The dynamical matrix D for planar graphene sheet is written in terms of the 3×3 matrices: (1) D^{AA} , (2) D^{AB} , (3) D^{BA} and (4) D^{BB}

for the coupling between (1) A and A, (2) A and B, (3) B and A and (4) B and B atoms in the various unit cells.

$$D = \begin{pmatrix} D^{AA} & D^{AB} \\ D^{BA} & D^{BB} \end{pmatrix} \quad 2.16$$

When we consider an A atom, the three nearest neighbor atoms (as shown in Figures 2.8(a) and 2.8(b)) are B_1 , B_2 and B_3 whose contributions to D are contained in D^{AB} , while the six nearest neighbor atoms contributions to D that are contained in D^{AA} and so on. The remaining problem is how to construct the force constant tensor K^{ij} . First the force constant between an A atom and a nearest neighbor B_1 atom on the x-axis as shown in Figure 2.8(b) has been considered. The force constant tensor is given by:

$$K^{(A,B_1)} = \begin{pmatrix} \phi_r^{(1)} & 0 & 0 \\ 0 & \phi_{ti}^{(1)} & 0 \\ 0 & 0 & \phi_{to}^{(1)} \end{pmatrix} \quad 2.17$$

where, $\phi_r^{(1)}$, $\phi_{ti}^{(1)}$ and $\phi_{to}^{(1)}$ represent the force constant parameters in the radial (bond stretching), in plane and out of plane tangential (bond bending direction) of the nearest neighbors, respectively. The force constant matrices for the two other nearest neighbor atoms, B_2 and B_3 are obtained by rotating the matrix in Equation 2.17.

$$K^{(A,B_m)} = U_m^{-1} K^{(A,B_1)} U_m \quad (m = 2,3) \quad 2.18$$

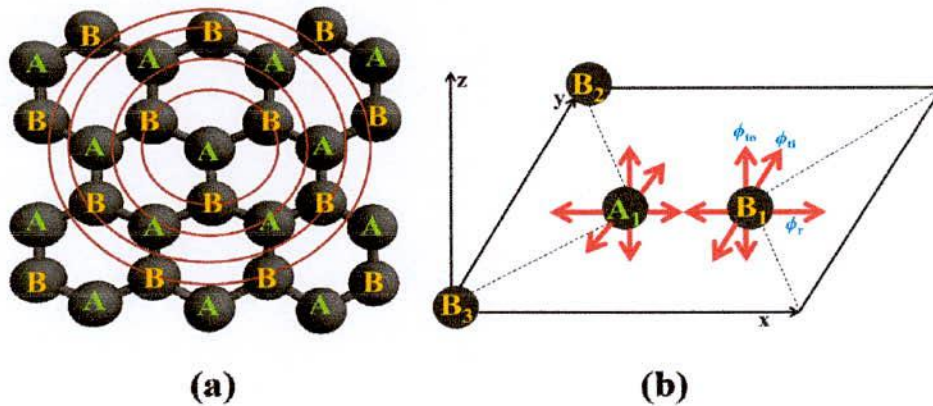


Figure 2.8 : (a) Neighbor atoms of graphene up to 4th nearest neighbors for A atom (similar results can be obtained for B atom). From the 1st to the 4th neighbor atoms, we plot solid circles. (b) Force constants between the A and B_1 atom on a planar graphene sheet. Here ϕ_r , ϕ_{ti} , and ϕ_{to} represent forces for the nearest neighbor atoms in the radial (bond stretching), in plane and out of plane tangential (bond bending) directions respectively. B_2 and B_3 are nearest neighbor equivalent to B_1 , whose force constant tensors are obtained by appropriately rotating the tensor for A and B_1 .

where the unitary matrix U_m is here defined by a rotating matrix around the z -axis in Figure 2.8(b), taking the B_1 atom into the B_m atom.

$$U_m = \begin{pmatrix} \cos\theta_m & \sin\theta_m & 0 \\ -\sin\theta_m & \cos\theta_m & 0 \\ 0 & 0 & 1 \end{pmatrix} \quad 2.19$$

To make the method explicit, the force constant matrix for the B_2 atom at $[-a/(2\sqrt{3}), a/2, 0]$, and U_2 is evaluated assuming $\theta_2 = \frac{2\pi}{3}$.

$$K^{(A,B_2)} = \frac{1}{4} \begin{pmatrix} \phi_r^{(1)} + 3\phi_{ti}^{(1)} & \sqrt{3}(\phi_{ti}^{(1)} - \phi_r^{(1)}) & 0 \\ \sqrt{3}(\phi_{ti}^{(1)} - \phi_r^{(1)}) & 3\phi_r^{(1)} + \phi_{ti}^{(1)} & 0 \\ 0 & 0 & \phi_{to}^{(1)} \end{pmatrix} \quad 2.20$$

and the corresponding phase factor is given by $\exp[-iq_x a/(2\sqrt{3}) + iq_y a/2]$.

Figure 2.9 shows the calculated phonon dispersion curves along with the DOSs for planar graphene sheet using the FCM [62].

The zone folding technique is the same as that used in treating the electronic structure of carbon nanotubes. By superimposing the N cutting lines in the K_1 extended representation on the six phonon frequency surfaces in the reciprocal space of the graphene layer (see Figure 2.7). The corresponding 1D phonon energy dispersion relation $\omega_{1D}^{m\mu}$ for the nanotubes is given by:

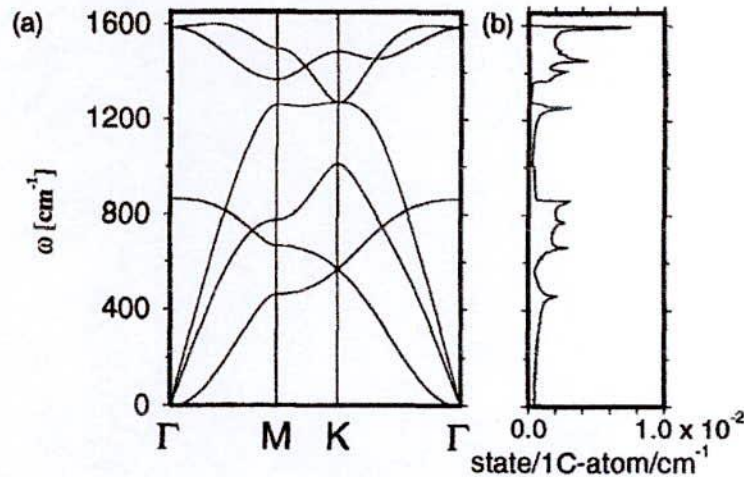


Figure 2.9 : (a) The phonon dispersion curves, plotted along high symmetry directions, for a 2D SWCNT sheet. (b) The corresponding DOSs vs phonon energy for phonon modes in units of states/l Catom/cm⁻¹ × 10⁻² [63].

$$\omega_{1D}^{m\mu} = \omega_{2D}^m \left(q \frac{K_2}{|K_2|} + \mu K_1 \right), \left(\begin{array}{l} m = 1, \dots, 6, \\ \mu = 0, \dots, N-1, \text{ and } -\frac{\pi}{T} < q \leq \frac{\pi}{T} \end{array} \right) \quad 2.21$$

where $\omega_{2D}^m(q)$ denotes the 2D phonon dispersion relations for a monolayer graphene sheet, q is a 1D wave vector, T is the magnitude of the 1D translation vector \mathbf{T} , and μ is a cutting line index.

According to the zone folding scheme, this procedure yields $6N$ phonon modes for each carbon nanotube. The $6(N/2-1)$ pairs of the phonon modes arising from the cutting lines of the indices μ and $-\mu$, where $\mu=1, \dots, (N/2-1)$, are expected to be doubly degenerate, similar to the case of the electronic sub-bands, while the phonon modes arising from the cutting lines for the indices $\mu=0$ and $\mu=N/2$ are non-degenerate. The total number of distinct phonon branches is $3(N+2)$.

Spikes appear in the PDOSs of the CNT, similar to the spikes Van-Hove singularities (VHSs) appearing in the electronic DOS (see Figure 2.10(b)), except for the presence of a much larger number of spikes in the phonon DOS than in the electronic DOS, due to the larger number of phonon modes relative to the number of electronic bands, and the more complex structure of the dispersion relations for phonons than for electrons in the graphene layer.

Figure 2.10 shows the calculated phonon dispersion curves along with the density of states for (10,10) ACNT using the FCM [63].

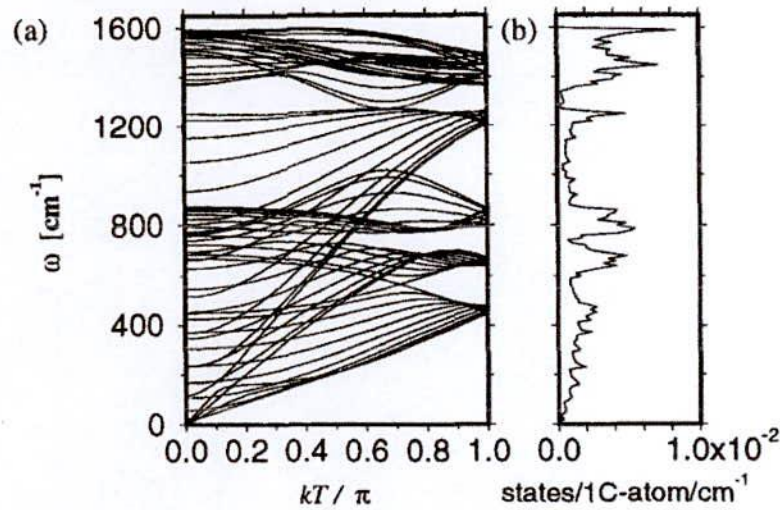


Figure 2.10 : (a) The calculated phonon dispersion relations of (10,10) ACNT. (b) PDOSs of (10,10) CNT [63].

2.6. Raman Spectroscopy

Raman spectroscopy has proven to be a powerful technique for probing selected phonons in SWCNT. Figure 2.11 shows Raman spectra of SWCNT. The Raman G peak measurement is a three step process (see Figure 2.12). (i) photon absorption leads to the excitation of an electron hole pair, (ii) relaxation of the electron (or the hole) via emission of a G phonon, and (iii) electron-hole recombination emits a red shifted photon. double resonance (DR) Raman scattering is a four step process (Figure 2.12), comprising (i) photon absorption, (ii) elastic defect scattering, (iii) inelastic electron phonon scattering, and (iv) electron hole recombination plus photon emission. The DR condition is reached when the energy is conserved in all these steps. Thus DR links the phonon wave vector to the electronic band structure [65].

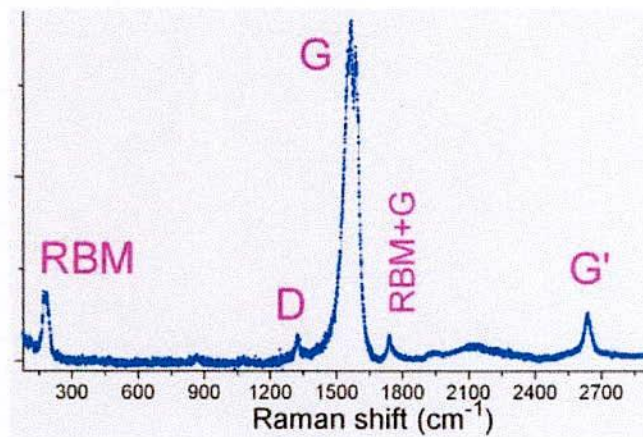


Figure 2.11 : Raman spectrum of SWCNT [65].

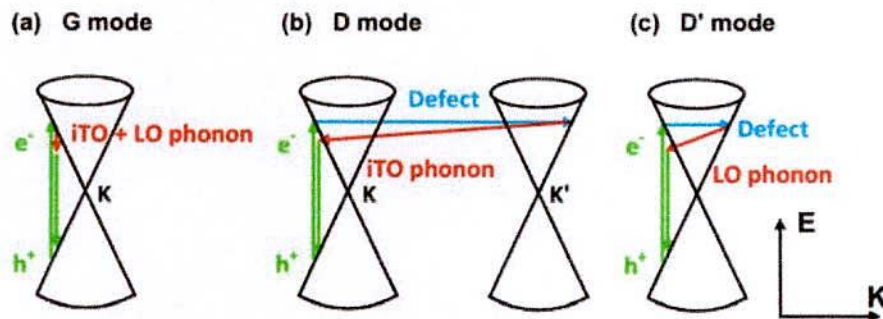


Figure 2.12 : Raman scattering process for (a) the G peak (in plane transverse optic (iTO) plus in plane longitudinal optic (iLO) mode). (b) Phonon double resonance process for the D peak (intervalley scattering) and (c) the D' peak (intravalley scattering) [58].

2.7 Vibrational Modes of SWCNT

Carbon nanotubes have many vibrational degrees of freedom because of the large number of atoms in their unit cells. Achiral tubes of $d \approx 1$ nm diameter have 100-150 phonon branches; in chiral nanotubes this number can be higher by one or two orders of magnitude. Only a very small fraction of these phonons is Raman active. The Raman active modes fall into a low-energy range where radial vibrations are observed, a high-energy range with in plane carbon-carbon vibrations, and an intermediate-frequency range. The low and high-energy phonons have received most attention; their Raman signal is very strong and they can be used for characterizing and studying CNTs as they give information about the tube diameter and chirality, phonon confinement, the semiconducting or metallic character, optical transition energies and more.

Carbon nanotubes are structures with particularly high symmetry. This comes from the underlying hexagonal lattice. The translations of graphene turn into rotational and helical symmetry operations for nanotubes, because we build the tube by rolling up graphene. The symmetry of carbon nanotubes was rigorously derived within the framework of line groups [66,67]. Line groups deal with systems that are periodic in one 1D. They are the equivalent of crystal space groups for 1D solids. The linegroup treatment is very powerful [68] for an introduction and for applications of the method to carbon nanotubes. From the point group and the positions of the carbon atoms, we thus obtain a total of 8 Raman active phonons in achiral and 15 in chiral nanotubes

$$\text{armchair } 2A_{1g} \oplus 2E_{1g} \oplus 4E_{2g} \quad 2.17$$

$$\text{zigzag } 2A_{1g} \oplus 3E_{1g} \oplus 3E_{2g} \quad 2.18$$

$$\text{chiral } 3A_1 \oplus 6E_1 \oplus 6E_2 \quad 2.19$$

Here A and B modes are nondegenerate, E modes have a twofold degeneracy. The A_{1g} , E_{1g} and E_{2g} representations are Raman active (the subscript g represents achiral tubes). The totally symmetric modes in achiral tubes are the radial breathing vibration and a high-energy phonon. In armchair tubes the circumferential eigenvector is Raman active and in zigzag tubes the axial vibration is Raman active. In chiral nanotubes, the three totally symmetric modes are the radial breathing mode (RBM) and two high-frequency vibrations. They resemble the circumferential and axial vibrations, but are, in general, of mixed character. This

is typical for low-dimensional systems; it originates from the mechanical boundary conditions (around the circumference in the case of nanotubes) [69-71].

2.7.1 Radial Breathing Mode

The RBM is an important mode for the characterization and identification of specific nanotubes, in particular of their chirality. Its eigenvector is purely radial by symmetry for armchair tubes only; these have mirror planes perpendicular to the nanotube axis, and the RBM is fully symmetric. For all other chiralities $n_1 \neq n_2$ the eigenvector has a small axial component, which is largest for zigzag tubes [72-74]. For most practical purposes, however, the RBM may be considered purely radial. RBM is Raman active mode in low-frequency region (see Figure 2.13).

2.7.2 Tangential Mode

Tangential modes refer to all phonon bands of a nanotube originating from the optical phonons of graphite. Their eigenvectors are characterized by an out of phase displacement of two neighboring carbon atoms. The displacement is directed parallel to the nanotube wall, along the circumference, the axis, or a direction in between. The tangential modes involve predominantly the sp^2 in plane carbon-carbon bonds, which are extremely strong, even stronger than in the sp^3 diamond bond. Therefore, these modes have very high frequencies lying between 1100 cm^{-1} and 1600 cm^{-1} (see Figure 2.13). The Raman active vibrations of the tangential modes fall into two groups, the high-energy modes (HEM) just below 1600 cm^{-1} and the D mode $\approx 1350 \text{ cm}^{-1}$. The HEM is also called the G line in the nanotube literature; the "G" originally stood for graphite and was taken over from the graphite Raman spectrum to CNTs. Another interesting optical phonon mode is D mode, which originate from defect induced SWCNT [68]. The name of G' mode is misleading: it is given because in graphite, this mode is usually the second strongest after the G mode. However, it is actually the second overtone of the defect induced D mode (and thus should logically be named D'). Its intensity is stronger than that of the D mode due to different selection rules [75]. In particular, D mode is forbidden in the ideal nanotube and requires a structural defect, providing a phonon of certain angular momentum, to be induced. In contrast, G' mode involves a "self-annihilating" pair of phonons and thus does not require defects. The spectral

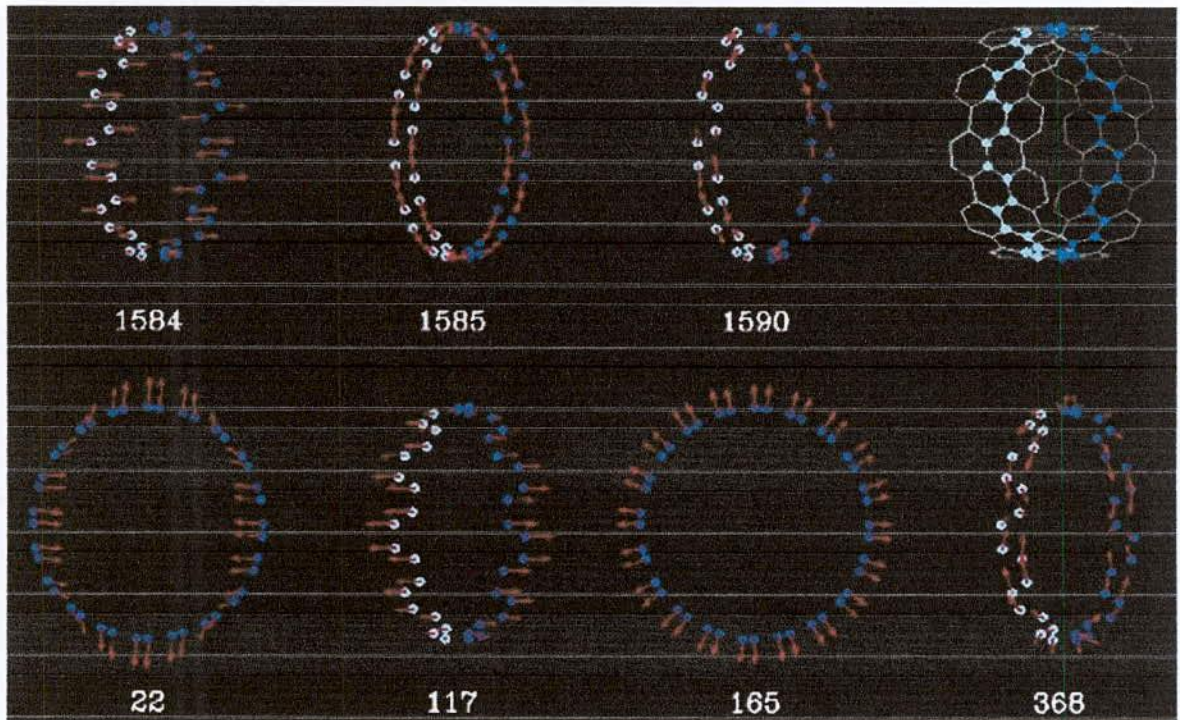


Figure 2.13 : Raman-active normal mode eigenvectors and frequencies for a (10,10) CNT. The red arrows indicate the magnitude and direction of the appropriate carbon atom displacements, and the eigenvectors shown correspond to the seven most intense modes. The unit cell (blue atoms) is shown schematically in the upper right-hand corner [28].

position of G' mode depends on diameter, so it can be used roughly to estimate the SWCNT diameter [77]. In particular, G' mode is a doublet in doublewall CNTs, but the doublet is often unresolved due to line broadening. Other overtones, such as a combination of RBM+G mode at $\sim 1750 \text{ cm}^{-1}$, are frequently seen in CNT Raman spectra. However, they are less important and are not considered here.

CHAPTER III

Computational Details

3.1 Introduction

This chapter outlines the numerical algorithm based on forced vibrational method used in the calculation of the later chapters.

3.2 Normal Modes of Vibration

Let us consider that a set of N atoms are coupled together by linear springs. The equation of motion of the systems with the scalar displacement of the l^{th} mass, $u_l(t)$ is:

$$M_l \ddot{u}_l + \sum_{l'} \phi_{ll'} u_{l'}(t) = 0 \quad 3.1$$

where M_l is the mass of l^{th} atom and $\phi_{ll'}$ is the strength of the spring between the l^{th} and l'^{th} atoms. The displacement can be decomposed as:

$$u_l(t) = \sum Q_\lambda(t) \frac{e_l(\lambda)}{\sqrt{M_l}} \quad 3.2$$

where Q_λ is the amplitude of the normal mode λ and $e_l(\lambda)$ is the displacement pattern or the polarization vector of the mode λ . By putting this value into Equation 3.1

$$M_l \frac{d^2}{dt^2} \left(\sum_\lambda Q_\lambda(t) \frac{e_l(\lambda)}{\sqrt{M_l}} \right) + \sum_{l'} \phi_{ll'} \sum_\lambda Q_\lambda(t) \frac{e_{l'}(\lambda)}{\sqrt{M_{l'}}} = 0 \quad 3.3$$

$$M_l \left(\sum_\lambda \ddot{Q}_\lambda(t) \frac{e_l(\lambda)}{\sqrt{M_l}} \right) + \sum_{l'} \phi_{ll'} \sum_\lambda Q_\lambda(t) \frac{e_{l'}(\lambda)}{\sqrt{M_{l'}}} = 0 \quad 3.4$$

Dividing this equation by $\sqrt{M_l}$, we have:

$$\sum_\lambda \ddot{Q}_\lambda(t) e_l(\lambda) + \sum_{l'} \phi_{ll'} \sum_\lambda Q_\lambda(t) \frac{e_{l'}(\lambda)}{\sqrt{M_l M_{l'}}} = 0 \quad 3.5$$

If the amplitude of the normal mode varies as $Q_\lambda(t) = A_\lambda \exp(i\omega_\lambda t) + B_\lambda \exp(-i\omega_\lambda t)$, after two times differentiation the equation of motion becomes:

$$-\omega_\lambda^2 \sum_\lambda (A_\lambda \exp(i\omega_\lambda t) + B_\lambda \exp(-i\omega_\lambda t)) e_l(\lambda) + \sum_{l'} \phi_{ll'} \sum_\lambda (A_\lambda \exp(i\omega_\lambda t) + B_\lambda \exp(-i\omega_\lambda t)) \frac{e_{l'}(\lambda)}{\sqrt{M_l M_{l'}}} = 0 \quad 3.6$$

Dividing the Equation 3.6 by $\sum_{\lambda} A_{\lambda} \exp(i\omega_{\lambda}t) + B_{\lambda} \exp(-i\omega_{\lambda}t) e_l(\lambda)$, we obtain:

$$\sum_{l'} \phi_{ll'} \frac{e_{l'}(\lambda)}{\sqrt{M_l M_{l'}}} = \omega_{\lambda}^2 e_l(\lambda) \quad 3.7$$

Thus, to find the frequencies and displacement patterns of the normal modes one has to find the eigenvalues and eigenvectors of an $N \times N$ matrix. However, the conventional dynamical matrix techniques require a large amount of computational time and huge memory space. These techniques are also limited for perfect system only. Thus, one has to find out another approach.

3.3 Forced Vibrational Method

The theoretical experiment we have done is based on the work by Williams and Maris [49]. The methodology they introduced is called FVM. This method is very efficient to find out the eigenvalues and eigenvectors of a large and complex harmonic physical system with mass disorder. The fundamental concept is based on the mechanical resonant effect of a physical system. When a system vibrating with random frequencies is continuously excited with an external periodic force of a particular frequency, Ω for sufficient time, the system will respond only with frequencies near Ω . Because this algorithm requires a memory space of the order of N , one can calculate eigenfrequencies and eigenmodes of a very large system.

If the desired lattice dynamical system consists of N number of atoms which are assumed to be coupled with linear springs with each other and the external force is applied to the system randomly, the resultant equation of motion will be as follows:

$$M_l \ddot{u}_l(t) + \sum_{l'} \phi_{ll'} u_{l'}(t) = F_l \cos(\Omega t) \quad 3.8$$

where M_l and u_l are the mass and scalar displacement of l^{th} atom respectively. $\phi_{ll'}$ represents the force constant between atoms l and l' . The periodic external force F_l is expressed as:

$$F_l = F_0 \sqrt{M_l} \cos(\varphi_l) \quad 3.9$$

where F_0 is time independent constant amplitude and the phase, φ_l is a random number distributed uniformly from 0 to 2π . The scalar displacement is composed of a set of normal modes according to the following expression:

$$u_l(t) = \sum_{\lambda} Q_{\lambda}(t) \frac{e_l(\lambda)}{\sqrt{M_l}} \quad 3.10$$

where $Q_{\lambda}(t)$ and $e_l(\lambda)$ are the amplitude and the displacement of the normal modes (λ),

respectively. To obtain the resonance condition, we have to establish time development algorithm of equation of motion as follows:

$$\dot{u}_l(n+1) = \dot{u}_l(n) + M_l^{-1} [\sum_{l'} \phi_{ll'} u_{l'}(n) + F_l \cos(\Omega n \tau)] \tau \quad 3.11$$

$$u_l(n+1) = u_l(n) + \dot{u}_l(n) \tau \quad 3.12$$

where the integer n is the number of time steps and total time, $= n\tau$. If we take τ sufficiently small, then we will get sharp resolution to extract the eigenmodes of the system. The value of τ must be satisfied the condition $\tau \leq \frac{\omega_m}{2}$, where ω_m is the maximum frequency of the system. From the above relation we can also find out the maximum frequency of the given sample system.

The total energy of the system can be written as the summation of kinetic and potential energy as follows:

$$\begin{aligned} E(t) &= K + U \\ &= \frac{1}{2} \sum_l M_l \dot{u}_l^2(t) + \frac{1}{2} \sum_l \sum_{l'} u_l(t) \phi_{ll'} u_{l'}(t) \end{aligned} \quad 3.13$$

at first, at time $t = 0$, all atoms are considered at rest with zero displacement. For $t > 0$, the external periodic force, F_l is applied to the each atom l . After completion of excitation time t , it is desirable that the system is in its resonance condition. Thus to obtain the DOSs around the frequency of the applied periodic force, we have to count the number of the excited eigenmodes, as the number of excited modes is directly related to the average energy of the sample system. When we average all possible values of ϕ_l and use the orthonormality of the eigenvectors $e_l(\lambda)$, the average value of energy $\langle E(\Omega) \rangle$ becomes as follows:

$$\langle E(\Omega) \rangle = \frac{\pi t F_0^2 N g(\Omega)}{8} \quad 3.14$$

where $g(\Omega)$ is the PDOSs. Therefore:

$$g(\Omega) = \frac{8 \langle E(\Omega) \rangle}{\pi t F_0^2 N} \quad 3.15$$

In order to obtain the DOS, our task is to compute the average total energy $\langle E \rangle$. Thus the DOS is independent of the frequency Ω of the applied force, but depends on the number of vibrational modes corresponding to the band of frequencies near the resonant frequency.

To obtain mode pattern of the given sample system, we have to apply the external force, F_l repeatedly to each atom l over an appropriate time interval T , until the amplitudes of

several eigenmodes belonging to frequencies close to Ω are enhanced enough. After one repetition of external force to each atom the displacement amplitude will be:

$$u_l^{(1)} = \frac{1}{\sqrt{M_l}} \sum_{\lambda} F_m e_l(\lambda) h^{(1)}(\Omega, \omega_{\lambda}, T) \quad 3.16$$

where ω_{λ} is an eigenfrequency of mode λ . Thus the new value of the force will be:

$$F_l^{(1)} = u_l^{(1)} M_l \quad 3.17$$

The system is again applied with a new force value $F_l^{(1)}$ to each atom considering each atom at rest. This process is repeated again and again until all the modes amplitudes died except the eigenmodes within the band of resonant frequency for appropriate values of time, T . After p times repetition the displacement amplitude will be as:

$$u_l^{(p)} = \frac{1}{M_l} \sum_{\lambda} F_m e_l(\lambda) h^{(p)}(\Omega, \omega_{\lambda}, T) \quad 3.18$$

$$\text{where } h(\Omega, \omega_{\lambda}, T) = \frac{2 \sin\left[\frac{1}{2}(\Omega - \omega_{\lambda})T\right] \sin\left[\frac{1}{2}(\Omega + \omega_{\lambda})T\right]}{\Omega^2 - \omega_{\lambda}^2} \quad 3.19$$

If we choose the value of p sufficiently large, the absolute value of the function h , expressed by Equation 3.19, will be maximized. Therefore, we will get maximum value of the displacements of the eigenmodes of the system. The above situation is determined by the frequency of the modes and is independent of the details of the driving forces, F . Thus, for sufficiently large p , we can rewrite the displacement amplitude Eq. 3.18 as:

$$u_l^{(p)} \approx \frac{C e_l(\lambda_l)}{\sqrt{M_l}} \quad 3.20$$

where C is a constant factor independent of λ . Thus, we can determine the mode pattern for the mode λ_l .

Now for obtaining the localization length we have to calculate inverse participation ratio *IPR* [77]. *IPR* can be mathematically expressed as:

$$IPR = \frac{\sum_{l=1}^N |u_{l,\lambda}|^4}{\left(\sum_{l=1}^N |u_{l,\lambda}|^2\right)^2} \quad 3.21$$

where $u_{l,\lambda}$ is the displacement of the l^{th} atom for the eigenmodes, λ . There are two particular types of phonon modes with special value of *IPR*. When a mode is localized, only a small number of atoms vibrate in that localized mode. If the number of atoms is m , that are vibrating with the localized mode, the vibrational amplitude of each atom is $u = \frac{1}{\sqrt{m}}$ taking the normalization of the eigenvector. Thus we can obtain inverse participation ratio from this

relationship and it is $IPR = \frac{1}{m}$. For the case $m=1$, we get the absolute localization mode condition, that is $IPR = 1$ and only one atom vibrates in that mode. For $m=N$ we get $IPR = \frac{1}{N}$ and in this situation all the atoms are in extended eigenmode with the same amplitude, $u = \frac{1}{\sqrt{N}}$. Therefore, by obtaining the value of IPR we can get the localization property of an eigenmode. The range of IPR is between $\frac{1}{N}$ to 1.

Now the relation between localization length and inverse participation ratio is $L_\lambda \propto IPR^{-\frac{1}{2}}$ [78]. We can then estimate the localization length of state, λ as:

$$\frac{L_\lambda}{L_0} = \left(\frac{IPR_0}{IPR_\lambda} \right)^{\frac{1}{2}} \quad 3.22$$

Where L_0 is the size of the system and IPR_0 is the average value of IPR_λ for the special case of pristine CNT sample.

3.4 Application of Force Vibrational Method to SWCNT

As an example of the application of the FVM to evaluate the vibrational states of the (10,0) and (10,10) SWCNTs honeycomb lattice has been demonstrated. The system treated here consists of N atoms which are connected to their nearest neighbors by the linear springs with force constant strength ϕ . As SWCNT honeycomb structure consists of two atoms (denoted by A and B) per unit cell, the different force directions can be observe for these two atoms. The force directions and the force constant tensors up to the fourth nearest neighbor atoms for the A type atoms for both (10,0) and (10,10) SWCNTs are illustrated in the Figure 3.1. In the same way, the force directions for the B type atoms can be determined. The angles (in degrees) between the central A atom and the different neighbor atoms up to the fourth nearest neighbor interactions for both (10,0) and (10,10) SWCNTs have been shown in the Table 3.1. In the same way, the angles for the B type atoms can be determined. The equations of motion for the (10,0) and (10,10) SWCNTs planar honeycomb lattices using the parameters listed in Table 3.1 are also demonstrated. Here the equations of motion of (10,0) and (10,10) CNTs for only first nearest neighbor atoms are derived. The equations can be derived for second, third and fourth nearest neighbor atoms by the similar way. In the same way, the equations can be derived for the B type atoms for both (10,0) and (10,10) CNTs.

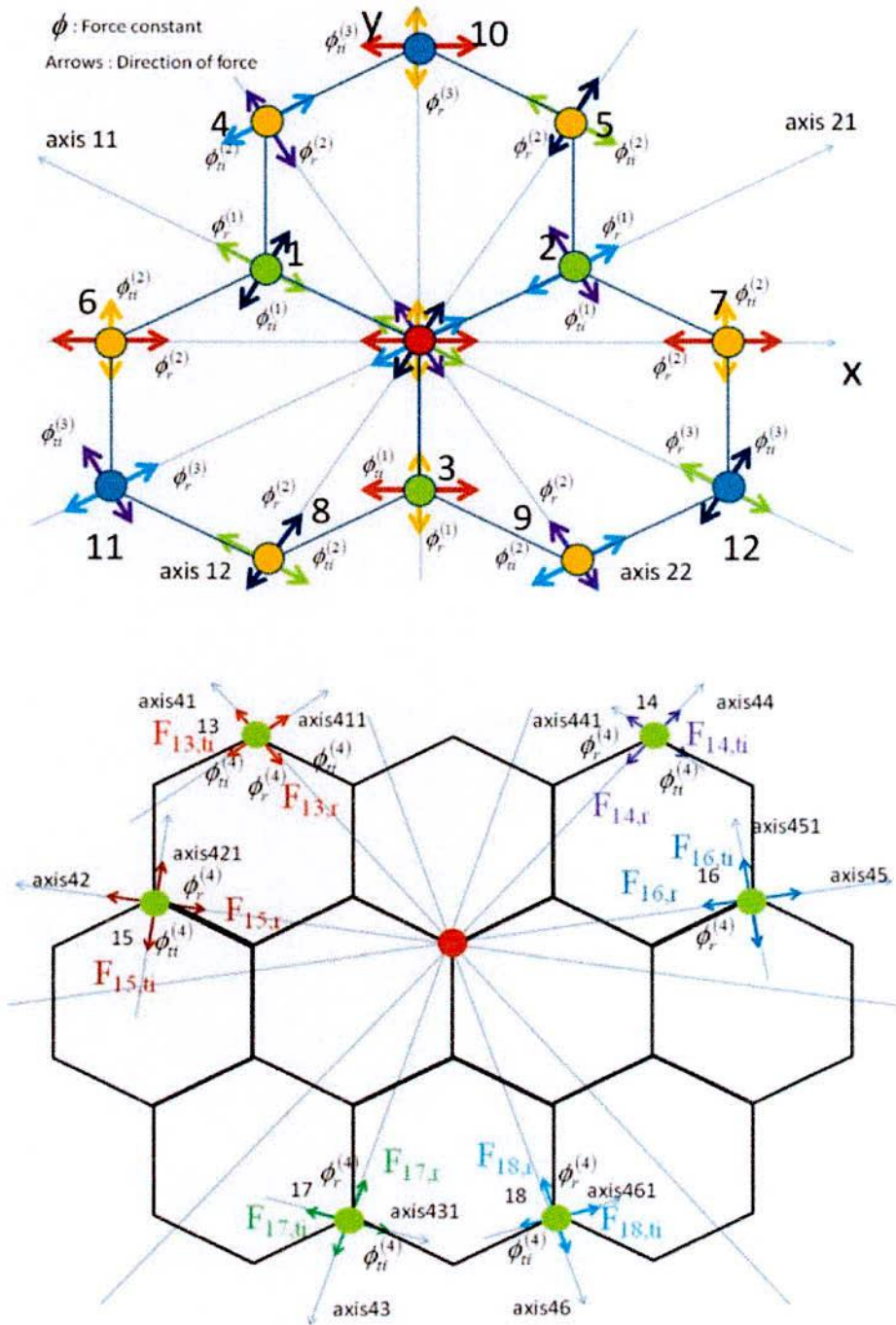


Figure 3.1 : A planar graphene sheet. The three shells of the nearest neighbors of the central A atom is shown by red circle. The directions of radial and tangential in plane force constant tensors are labeled by ϕ_r and ϕ_{tt} respectively. The central A atom and the three B atoms from the first shell are labeled by 1, 2 and 3. In the similar way, second and third shells are labeled by the consecutive numbers. For (10,0) ZCNT and (10,10) ACNT only the x and y-axis will be interchanged [58].

Table 3.1: The angles (in degrees) between the central A type atom and different neighbors for (10,0) ZCNT and (10,10) ACNT (only x and y-axis will be interchanged).

A type atom for (10,0) ZCNT						
Atom number	A			B		
	Angle		Nearest neighbor	Angle		Nearest neighbor
	Radial	Tangential		Radial	Tangential	
1			0	150	-120	1
2			0	30	-60	1
3			0	90	0	1
4	-60	30	2			0
5	-120	150	2			0
6	0	90	2			0
7	0	90	2			0
8	-120	150	2			0
9	-60	30	2			0
10			0	90	0	3
11			0	30	-60	3
12			0	150	-120	3
13			0	131	41	4
14			0	49	-41	4
15			0	169	79	4
16			0	11	-79	4
17			0	-109	-19	4
18			0	-71	19	4
A type atom for (10,10) ACNT						
Atom number	A			B		
	Angle		Nearest neighbor	Angle		Nearest neighbor
	Radial	Tangential		Radial	Tangential	
1			0	60	-30	1
2			0	120	-150	1
3			0	0	90	1
4	-150	120	2			0
5	-30	60	2			0
6	90	0	2			0
7	90	0	2			0
8	-30	60	2			0
9	-150	120	2			0
10			0	0	90	3
11			0	120	-150	3
12			0	60	-30	3
13			0	41	131	4
14			0	139	-131	4
15			0	79	169	4
16			0	101	-169	4
17			0	-19	-109	4
18			0	-161	109	4

The equations of motion for the SWCNT planar honeycomb lattices:

For A type atom in (10,0) CNT (first nearest neighbours):

$$v_{l,x}(n+1) = v_l(n) + M_l^{-1}[\phi_r^1(u_{l,1} - u_l)\cos(150)^\circ + \phi_{ti}^1(u_{l,1} - u_l)\cos(-120)^\circ + \phi_r^1(u_{l,2} - u_l)\cos(30)^\circ + \phi_{ti}^1(u_{l,2} - u_l)\cos(-60)^\circ + \phi_r^1(u_{l,3} - u_l)\cos(90)^\circ + \phi_{ti}^1(u_{l,3} - u_l)\cos(0)^\circ + F_{l,x}\cos(\Omega n\tau)]\tau \quad 3.23$$

$$v_{l,y}(n+1) = v_l(n) + M_l^{-1}[\phi_r^1(u_{l,1} - u_l)\sin(150)^\circ + \phi_{ti}^1(u_{l,1} - u_l)\sin(-120)^\circ + \phi_r^1(u_{l,2} - u_l)\sin(30)^\circ + \phi_{ti}^1(u_{l,2} - u_l)\sin(-60)^\circ + \phi_r^1(u_{l,3} - u_l)\sin(90)^\circ + \phi_{ti}^1(u_{l,3} - u_l)\sin(0)^\circ + F_{l,y}\cos(\Omega n\tau)]\tau \quad 3.24$$

$$v_{l,z}(n+1) = v_l(n) + M_l^{-1}[\phi_r^1(u_{l,1} - u_l) + \phi_{ti}^1(u_{l,1} - u_l) + \phi_r^1(u_{l,2} - u_l) + \phi_{ti}^1(u_{l,2} - u_l) + \phi_r^1(u_{l,3} - u_l) + \phi_{ti}^1(u_{l,3} - u_l) + F_{l,z}\cos(\Omega n\tau)]\tau \quad 3.25$$

For A type atom in (10,10) CNT (first nearest neighbours):

$$v_{l,x}(n+1) = v_l(n) + M_l^{-1}[\phi_r^1(u_{l,1} - u_l)\cos(60)^\circ + \phi_{ti}^1(u_{l,1} - u_l)\cos(-30)^\circ + \phi_r^1(u_{l,2} - u_l)\cos(120)^\circ + \phi_{ti}^1(u_{l,2} - u_l)\cos(-150)^\circ + \phi_r^1(u_{l,3} - u_l)\cos(0)^\circ + \phi_{ti}^1(u_{l,3} - u_l)\cos(90)^\circ + F_{l,x}\cos(\Omega n\tau)]\tau \quad 3.26$$

$$v_{l,y}(n+1) = v_l(n) + M_l^{-1}[\phi_r^1(u_{l,1} - u_l)\sin(60)^\circ + \phi_{ti}^1(u_{l,1} - u_l)\sin(-30)^\circ + \phi_r^1(u_{l,2} - u_l)\sin(120)^\circ + \phi_{ti}^1(u_{l,2} - u_l)\sin(-150)^\circ + \phi_r^1(u_{l,3} - u_l)\sin(0)^\circ + \phi_{ti}^1(u_{l,3} - u_l)\sin(90)^\circ + F_{l,y}\cos(\Omega n\tau)]\tau \quad 3.27$$

$$v_{l,z}(n+1) = v_l(n) + M_l^{-1}[\phi_r^1(u_{l,1} - u_l) + \phi_{ti}^1(u_{l,1} - u_l) + \phi_r^1(u_{l,2} - u_l) + \phi_{ti}^1(u_{l,2} - u_l) + \phi_r^1(u_{l,3} - u_l) + \phi_{ti}^1(u_{l,3} - u_l) + F_{l,z}\cos(\Omega n\tau)]\tau \quad 3.28$$

3.5 Correction of Force Constants

The CNT can be assumed as rolled version of planar graphene sheet. To determine the phonon dispersion relation and ultimately the PDOs of SWCNT, we have used the force constants up to fourth nearest neighbors given by Jishi et al. [64]. These values for force constants are obtained by fitting the 2D phonon dispersion relation over the Brillouin zone as

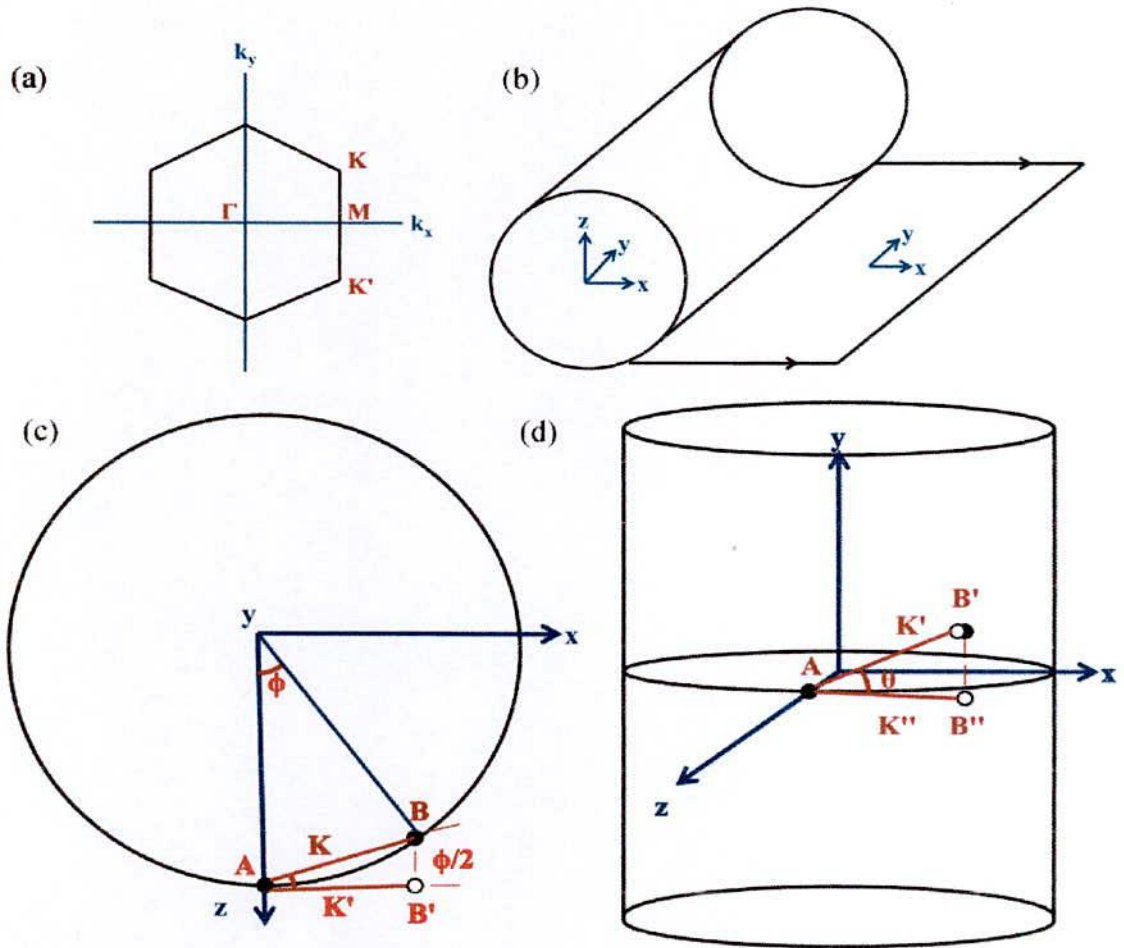


Figure 3.2 : (a) Brillouin zone of CNT with high symmetry points (b) Obtaining two dimensional graphene sheet from cylindrical CNT, chiral vector is along x-axis and translational vector along y-axis (c) (Top view of CNT) projection of B (filled circle) atom on xy-plane denoted as B' (unfilled circle) (d) (Side view of CNT) projection of B' (unfilled circle) on zx-plane denoted as B'' (unfilled circle).

determined experimentally, as for example for from inelastic neutron scattering or electron energy loss spectroscopy measurements along the ΓM direction. In Figure 3.2(a) the Brillouin zone of CNT with high symmetry points such as Γ , K and M points are shown.

As CNT is cylindrical in shape, we have to consider the curvature effect on these force constants. First, we have determined the circumferential length for both CNT from their absolute value of chiral vectors as follows:

$$L = |C_h| = a\sqrt{n^2 + nm + m^2} \quad 3.29$$

where a is the lattice constant and $a = 1.42\sqrt{3} = 2.46 \text{ \AA}$. n, m are integers, $0 \leq |m| \leq n$. We also have calculated the translation vectors for both CNTs as follows:

$$T = |T| = \frac{\sqrt{3}L}{d_R} \quad 3.30$$

where d_R is the greatest common divisor of $(2n + m)$ and $(2m + n)$.

The product of chiral vector and translational vector is the unit cell of the CNT [62]. After sufficient repetitions of translational vector, the required length of CNT is obtained. Here we have repeated the translational vector 250 times and got 10,000 carbon atoms for both (10,0) and (10,10) CNTs.

Now from Figure 3.2(b), it is shown that chiral vector is in the direction of circumference of CNT and translational vector is in the direction of the axis of the CNT (here it is in the y -axis direction). After unfolding the CNT we get 2D planar graphene sheet. Its width is same as the circumferential length of the chiral vector (here it is now in the x -axis direction) and length is same as the length of repeated translational vector (here it is in the y -axis direction) of the corresponding CNT.

The change in atomic positions in the flat graphene plane with respect to the curved CNT wall has been incorporated by explicitly including the change in bond angle on the planar graphene sheet. To obtain the curvature effect, we have followed the following procedure as shown in Figures. 3.2(c) and 3.2(d). Let consider, two atoms A and B. The force constant between them is K as shown in Figure 3.2(c). At first we take projection of B (filled circle) on xy -plane denoted by B' (unfilled circle). The new value of force constant tensor K is K' . The rotation angle between K and K' around y -axis is $\phi/2$. Where ϕ is the angle between A and B atoms at the center. Then we have taken projection of B' (unfilled circle) on zx -plane denoted by B'' (unfilled circle) according to Figure 3.2(d). The new component of K is K'' . Where K'' is parallel to the direction of the x -axis.

To determine ϕ , the angle between A and B at the center, we have to consider the following equation:

$$\phi = \cos^{-1} \left\{ \frac{2r^2 - |P_i - P_j|^2}{2r^2} \right\} \quad 3.31$$

where r is the radius of the SWCNT, P_i is the i^{th} atom which we consider and P_j is the j^{th} nearest neighbor atom. If we consider carbon-carbon bond length 1.42 \AA , the radius r of (10,0) ZCNT is found $r_{(10,0)} = 3.91 \text{ \AA}$ and (10,10) ACNT is found $r_{(10,10)} = 6.78 \text{ \AA}$.

Table 3.2 shows the distances between 1st, 2nd, 3rd, 4th nearest neighbours carbon-carbon atoms in SWCNT without considering curvature effect. Table 3.3 shows the value of angles ϕ between nearest neighbor atoms of (10,0) and (10,10) CNT.

Table 3.2 : The obtained nearest neighbor distances without curvature effect.

Nearest neighbors (P_j)	Distances $ P_i - P_j $
1 st (P_1)	1.42 Å
2 nd (P_2)	2.46 Å
3 rd (P_3)	2.84 Å
4 th (P_4)	3.69 Å

Table 3.3 : The obtained angles between A and B atoms.

Nearest neighbors (P_j)	ϕ (10,0) CNT	ϕ (10,10) CNT
1 st (P_1)	20.90 ⁰	12.02 ⁰
2 nd (P_2)	36.62 ⁰	20.90 ⁰
3 rd (P_3)	42.54 ⁰	24.18 ⁰
4 th (P_4)	56.23 ⁰	31.57 ⁰

Table 3.4 : The obtained force constants values taking into account the curvature effect.

Force constants	Jishi et al.[64]	Our calculated force constants for (10,0) CNT	Our calculated force constants for (10,10) CNT
$K_r^{(1)}$	365.00	358.95	363.00
$K_r^{(2)}$	88.00	83.54	86.54
$K_r^{(3)}$	30.00	27.96	29.33
$K_r^{(4)}$	-19.20	-16.93	-18.48
$K_{ii}^{(1)}$	245.00	240.94	243.65
$K_{ii}^{(2)}$	-32.30	-30.66	-31.76
$K_{ii}^{(3)}$	-52.50	-48.92	-51.34
$K_{ii}^{(4)}$	22.90	20.20	22.04
$K_{to}^{(1)}$	98.20	96.57	97.66
$K_{to}^{(2)}$	-4.00	-3.80	-3.93
$K_{to}^{(3)}$	1.50	1.40	1.47
$K_{to}^{(4)}$	-5.80	-5.12	-5.58

The force constants between two carbon atoms are taken from the report by Jishi et al. [64] and the only interactions up to the fourth nearest neighbor atoms are considered in this work. Our calculated force constants considering curvature effect are shown in Table 3.4 for both (10,0) and (10,10) CNTs. The calculated force constants are found multiplying with factor $\cos(\phi/2)$.

3.6 Periodic Boundary Condition

As CNT is cylindrical in shape, we have to apply PBC along the chiral vector direction. To apply PBC to a matrix, we assume that the last point is connected back to the first point so that there are no ends (see Figure 3.3). The justification for this assumption is that if we are interested in the properties in the interior of a structure in a cylindrical crystal system, then what we have to assume at the boundaries should make no real difference and we could assume anything to make our calculations simpler.

In Figure 3.4, an unfold zigzag (here we take it for describing (10,0) CNT) CNT with vacancy defects is shown. After unfolding there are N numbers of lines are found depending

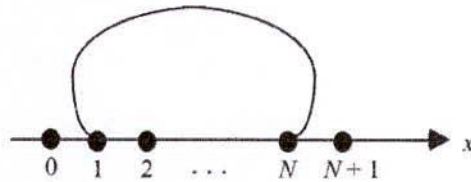


Figure 3.3 : PBC assume that there are no “ends.” Point N is connected back to point 1 as if the structure were in the form of a ring making $(N+1)$ equivalent to 1 [79].

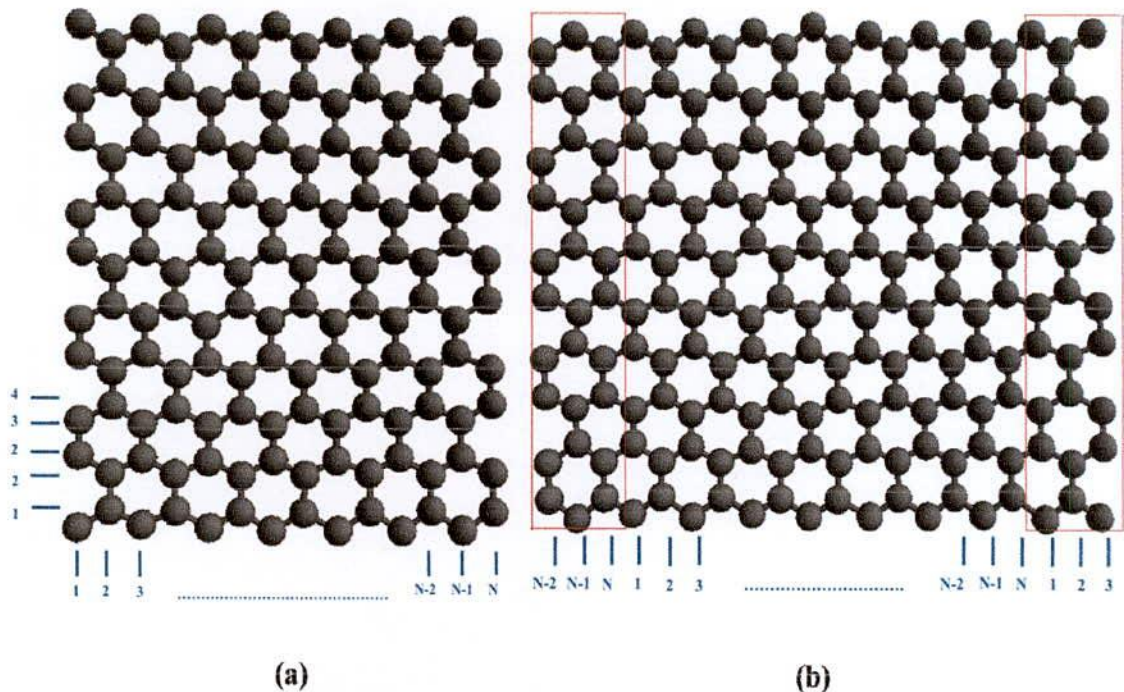


Figure 3.4 : (a) Unfolded (10,0) SWCNT (b) Application of PBC.

of chirality. These lines are numbered in the chiral direction. To obtain PBC along the chiral vector we have taken first three line (1,2,3) at the end of the line numbered as N . We also have taken last three lines ($N-2,N-1,N$) before the line numbered as 1 as illustrated in Figure 4.2. The repeated lines are shown within red rectangle. We repeated first and last three lines because in applying FVM we have considered force constants up to fourth nearest neighbors. So that it is sufficient to take three lines at each side. In Table 3.5 A sample matrix is shown to apply PBC. This matrix represent the atoms of unfolded (10,0) SWCNT of Figure 3.4.

Table 3.5 : Sample matrix element of (10,0) SWCNT of Figure 3.4. Here 1 and 0 represent the presence of atoms and absence of atoms respectively.

	8	9	10	2	3	4	5	6	7	8	9	10	2	3	4
1	1	0	1	1	0	1	0	1	0	1	0	1	1	0	1
2	1	1	1	1	1	1	1	1	1	1	1	1	1	1	1
3	0	1	0	0	1	0	1	0	1	0	1	0	0	1	0
4	1	0	1	1	0	1	0	1	0	1	0	1	1	0	1
5	1	1	1	1	1	1	1	1	1	1	1	1	1	1	1
6	0	1	0	0	1	0	1	0	1	0	1	0	0	1	0
7	1	0	1	1	0	1	0	1	0	1	0	1	1	0	1
8	1	1	1	1	1	1	1	1	1	1	1	1	1	1	1
9	0	1	0	0	1	0	1	0	1	0	1	0	0	1	0

3.7 Creation of Atomic Vacancies

The atomic vacancy defects are created randomly using percolation theory. Percolation theory discuss the formation of long range connectivity in random systems. It generally refers to simplified lattice models of random systems or networks and the nature of the connectivity in them [80]. The percolation model is used here is a lattice, like honeycomb lattice, and make it into a random network by randomly "occupying" sites (vertices) or bonds (edges) with a statistically independent probability p (see Figure 3.5). At a critical threshold p_c , large clusters and long range connectivity first appears, and this is called the percolation threshold. Depending on the method for obtaining the random network, one distinguishes between the site percolation threshold and the bond percolation threshold. We have considered vacancy concentrations up to 30%, because the percolation threshold of a site percolation network of

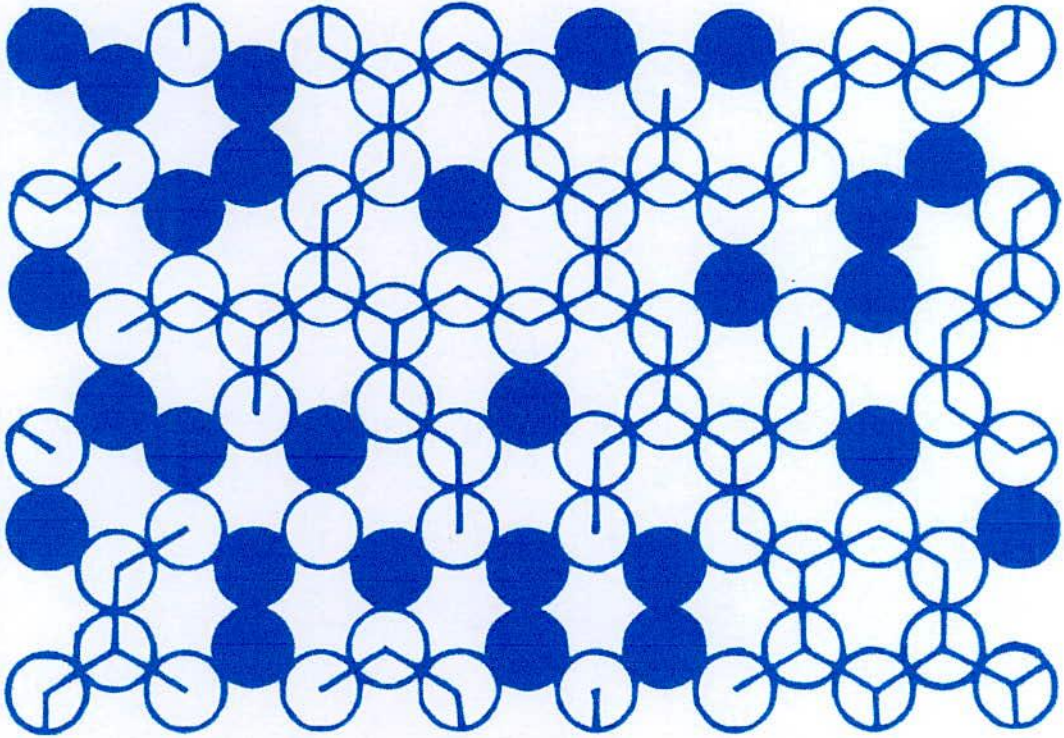


Figure 3.5 : Example of disorder percolation network of honeycomb lattice [81].

honeycomb lattice is about 70% [82]. The total number of carbon atoms we have taken for both (10,0) ZCNT and (10,10) ACNT is 10,000. As both (10,0) and (10,10) CNTs have 40 carbon atoms per unit cell, the total number of unit cells are taken 250 for both CNTs. The length of (10,0) and (10,10) CNTs, we have taken here are 61.50 nm and 106.50 nm respectively, because in modern scaled nanoelectronic devices, ballistic transport of carrier can be achieved over length typically less than 100 nm [83]. The diameters of (10,0) and (10,10) CNTs are 0.78 nm and 1.36 nm respectively. Our simulations have been performed considering PBC along chiral direction.

CHAPTER IV

Results and Discussion

4.1 Introduction

In this chapter, the results of the computer experiment on the phonon properties of (10,0) ZCNT and (10,10) ACNT considering the effects of vacancy type defects and curvature for a large number of lattices has been presented. The FVM has been applied to describe the change in the PDOSs due to the vacancy type defects and curvature. To study the nature of phonon states, the typical mode pattern in the presence of vacancy type defects has been calculated. This work focuses particularly on the K point Γ TO mode phonons because of their importance in the Raman D-band, the dominant feature in the Raman spectra for a defective crystal system. Moreover, the localization length as a function of vacancy type defect density has also been computed to study the localization effects caused by vacancy type of disorder. Figure 4.1 shows vacancy induced SWCNTs considered in this work.

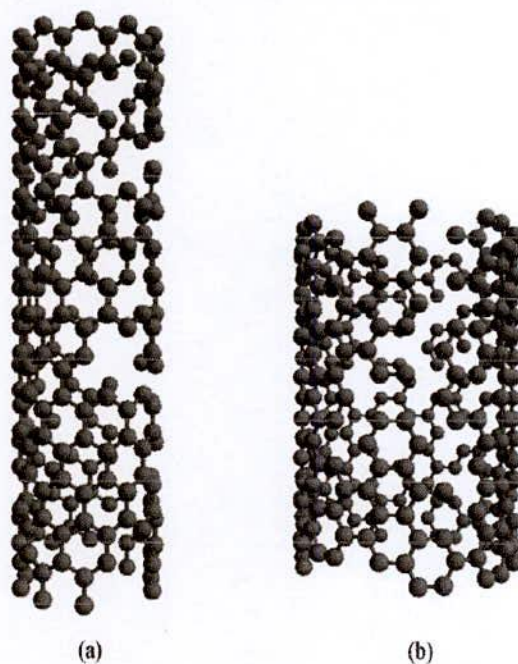


Figure 4.1 : Vacancy (about 30%) induced defective CNTs. (a) (10,0) semiconducting ZCNT and (b) (10,10) ACNT.

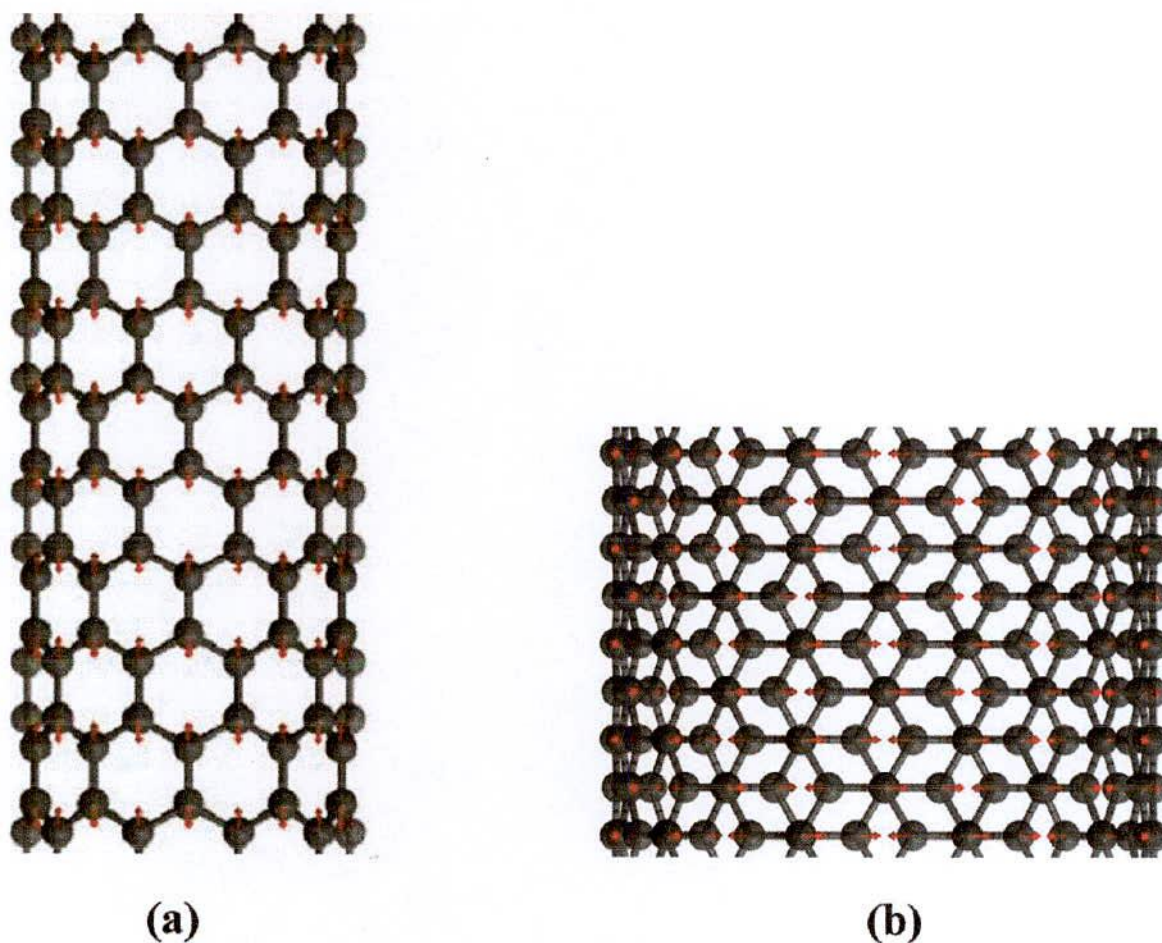


Figure 4.2 : Raman active E_{2g} phonon mode direction at Γ point of Brillouin zone of (a) (10,0) CNT (b) (10,10) CNT (red arrows).

4.2 Phonon Density of States of SWCNT

In this work I have calculated PDOSs of (10,0) ZCNT and (10,10) ACNT using FVM, considering force constants up to fourth nearest neighbor atoms. It is well known that both (10,0) and (10,10) CNTs have $2N=40$ carbon atoms per unit cell, where N is the number of hexagons per unit cell. Thus both the CNTs should have $6N$ vibrational degree of freedom and $6N$ distinct phonon branches. In case of low dimensional material like CNT due to mode degeneracy, $6N$ distinct phonon branches do not always exist. For example, in (10,10) CNT there are only 66 distinct phonon branches with respect to the phonon eigenvectors at the Brillouin zone center Γ point, of which 12 modes are non-degenerate and 54 modes are degenerate [84]. The iLO and iT0 modes, which are the main focus of this work, involve

predominantly the sp^2 in-plane carbon-carbon bonds and these bonds are extremely strong, even stronger than the sp^3 diamond bonds. Therefore, these vibrational modes have very high frequencies lying between 1100 cm^{-1} and 1600 cm^{-1} . Among these high frequency in-plane tangential vibrational modes, the Raman active modes fall into two groups, the G modes just below 1600 cm^{-1} and the D modes around 1350 cm^{-1} . In CNT the TO phonon mode is the highest G band phonon modes just opposite to graphene. For (10,0) semiconducting ZCNT iLO phonon mode and (10,10) metallic ACNT iTO phonon mode are Raman active and they are responsible for E_{2g} mode at the Brillouin zone center as shown in Figures 4.2(a) and 4.2(b) (red arrows) [28,65,85].

The simulated PDOSs of perfect CNTs exhibit 1D VHSs because of confinement effect originated from the reduced dimensionality and all the characteristic peaks that correspond to the sp^2 bonded carbon honeycomb lattice as shown in Figures 4.3(a) and 4.3(b). In this simulation I have found the E_{2g} mode at 1576 cm^{-1} and 1581 cm^{-1} for (10,0) and (10,10) CNTs respectively. Generally the E_{2g} mode gives a large softening due to curvature effect [63]. Again the LO phonon mode whose atomic displacement direction is along the axial direction of CNT is less sensitive to curvature effect and the TO phonon mode whose atomic displacement direction is along the circumferential direction of CNT is more sensitive to curvature effect [40]. As the diameter of (10,0) ZCNT is much less than (10,10) ACNT, the curvature effect is more severe in (10,0) ZCNT compared to (10,10) ACNT. Thus, it is reasonable to find the E_{2g} mode at lower frequency for (10,0) ZCNT than (10,10) ACNT. It is worth to mention here that some previous works found E_{2g} mode for graphene and graphene nanoribbon at 1590 cm^{-1} using FVM [86,87]. Moreover, graphene and graphene nanoribbon have no curvature effect. From the PDOSs of pristine CNTs, it is found that the average high energy PDOS is less for (10,10) CNT than (10,0) CNT. Due to Khon anomaly in the (10,10) metallic CNT, the LO phonon modes soften towards the lower frequency range [39,40].

I also have simulated the PDOS of (10,0) and (10,10) CNTs for a broad range of vacancy concentrations changes. It is found that vacancy type defects have significant effects on PDOSs of both CNTs. These results show that the broadening and softening of the PDOSs peaks as the defect density increases for both CNTs. It is found that E_{2g} mode softening effect is stronger in (10,0) than (10,10) CNT due to curvature effect as illustrated in Figure 4.4. The reason behind the shifting of the PDOSs peaks towards the low-frequency region for both

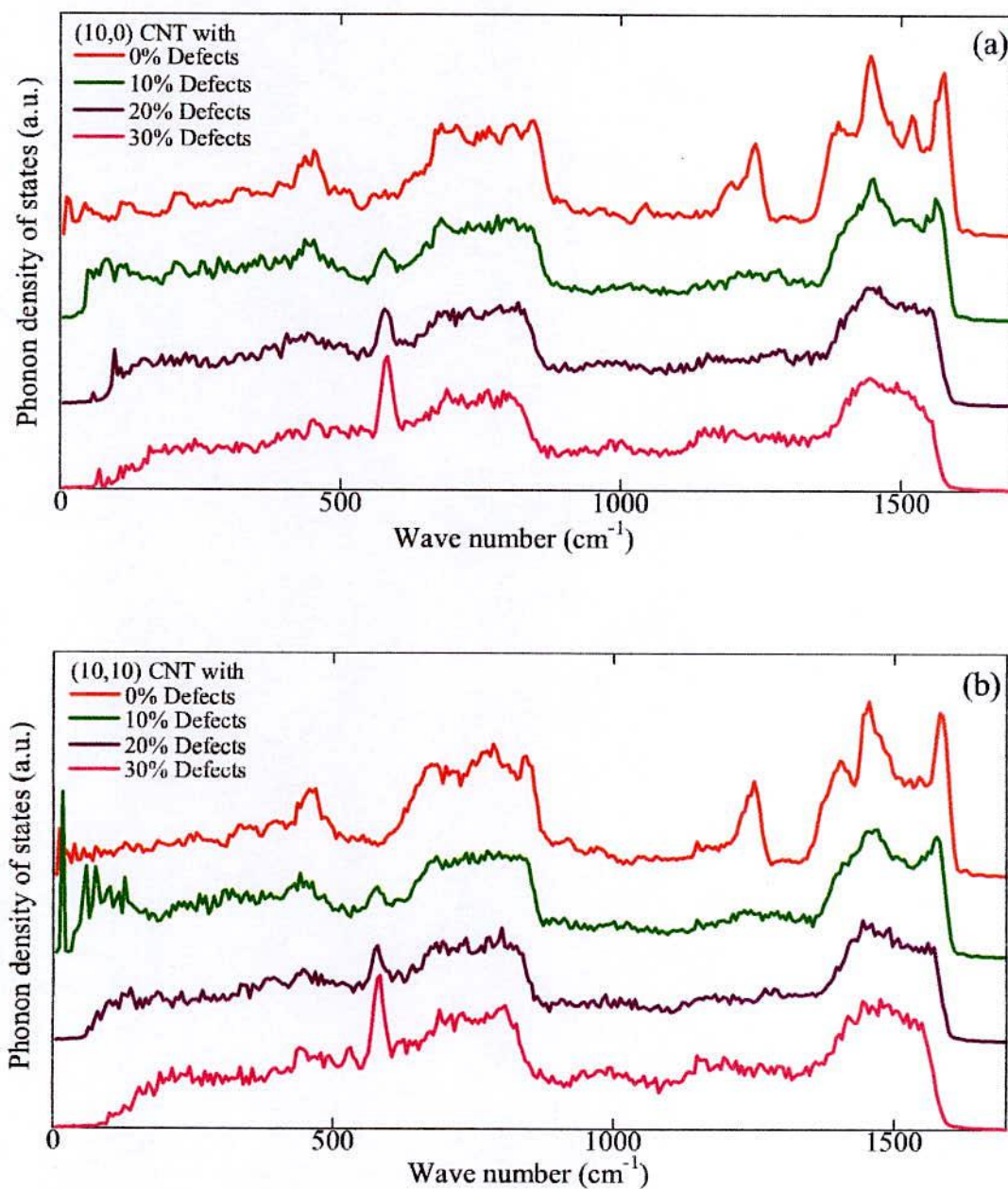


Figure 4.3 : PDOSs of (a) (10,0) CNT (b) (10,10) CNT with variation of vacancy concentration over 0% - 30%.

cases can be explained as, with increasing defect densities the numbers of the unsaturated carbon atoms with some dangling bonds increase. As the bonding strength is weak for the unsaturated carbon atoms, the PDOSs of CNTs shift down towards low-frequency region from

high-frequency region. Another significant outcome of this simulation is that the E_{2g} peak has been reduced into a shoulder, or it has completely disappeared for vacancy concentrations of 10% and higher in both cases. This result interprets that when atomic vacancies are present in a crystal system, after increasing certain value of defect densities the long range periodic order of that crystalline system is totally perturbed. Moreover, the momentum conservation is broken down because of breaking the translational symmetry of the crystalline arrangement of CNTs. That is why it is found that some fine structures are disappeared in high-frequency region of PDOSs for both CNTs.

Another interesting property that have found in PDOSs of both CNTs is the appearance of some fine peaks in the low-frequency region with the increase in defect density. Mingo et al. [88] explained that the presence of defects efficiently scatters longer wavelength phonons. Recently Sevik et al. [89] found that in spite of increasing vacancy defects, low-frequency phonons are transmitted quasi ballistically in CNTs. So the fine peaks may be the result of these facts. Although some fine peaks appear in the low-frequency region with the increase in defect densities, the average PDOSs in the low-frequency region has been reduced for both types of CNTs with increasing defect densities. Mahan et al. [90] have reported that there

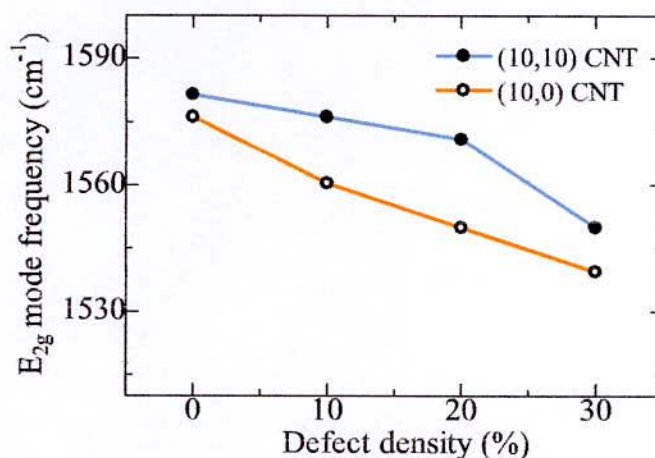


Figure 4.4 : Comparison of softening of Raman active E_{2g} mode of (10,0) and (10,10) CNTs with increasing defect densities.

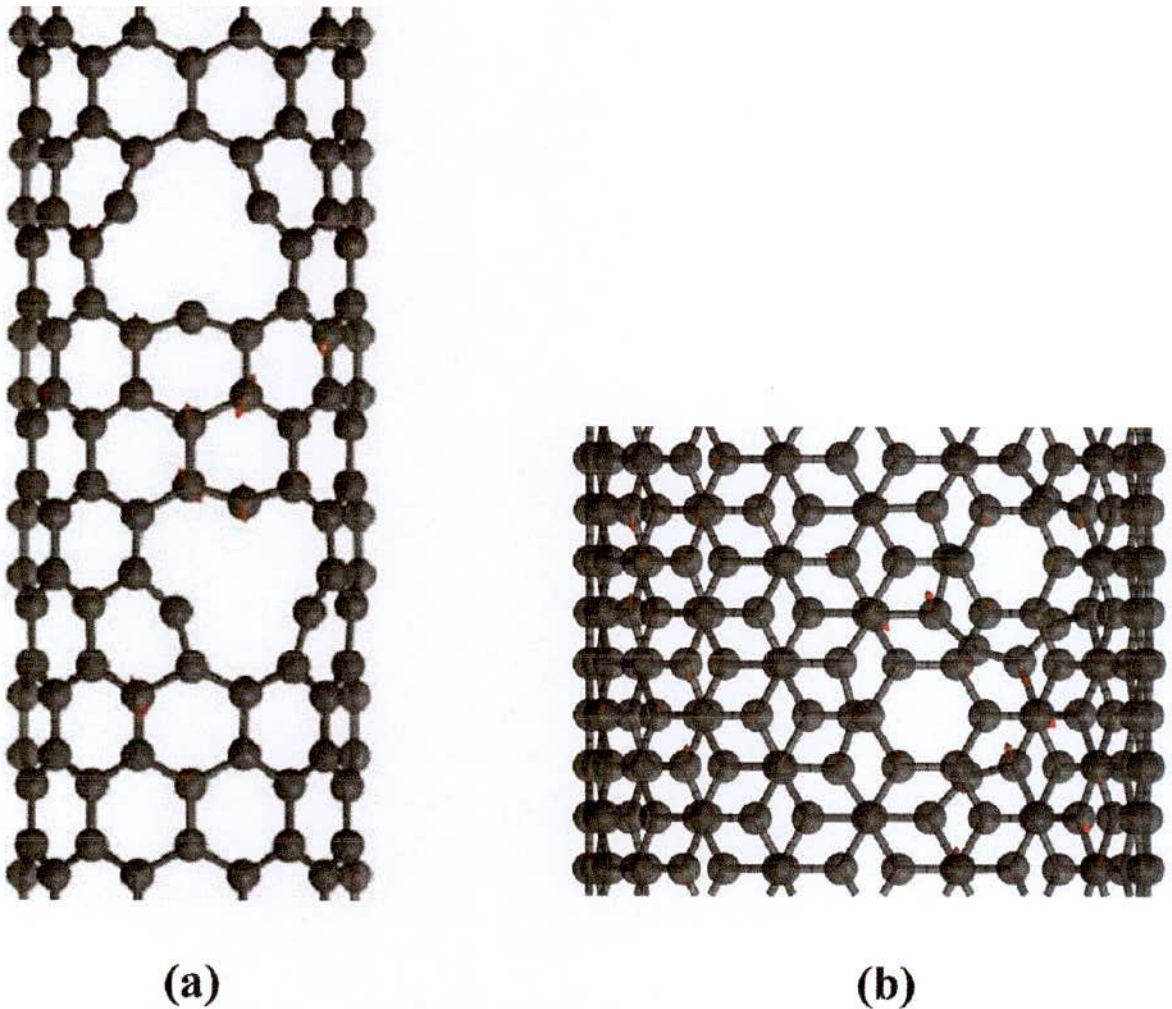


Figure 4.5 : Vibrational direction of D-band mode at K point of Brillouin zone of defective (a) (10,0) CNT (b) (10,10) CNT (red arrows).

exists flexural phonon modes in low frequency acoustic PDOS region of the CNT, which shows the quadratic phonon dispersion relation and recently Ochoa et al. [91] have showed that a reduction in the value of PDOS of graphene due to stiffening of the flexural phonon modes with inducing defects in the sample system. It is predicted that these are the factors behind the reduction of average PDOSs in the low-frequency region.

4.3 Mode Pattern of SWCNT

In this work, I also have analyzed vacancy defects effect on phonon localization. The phonon wave function is considered delocalized in carbon-based low dimensional materials.

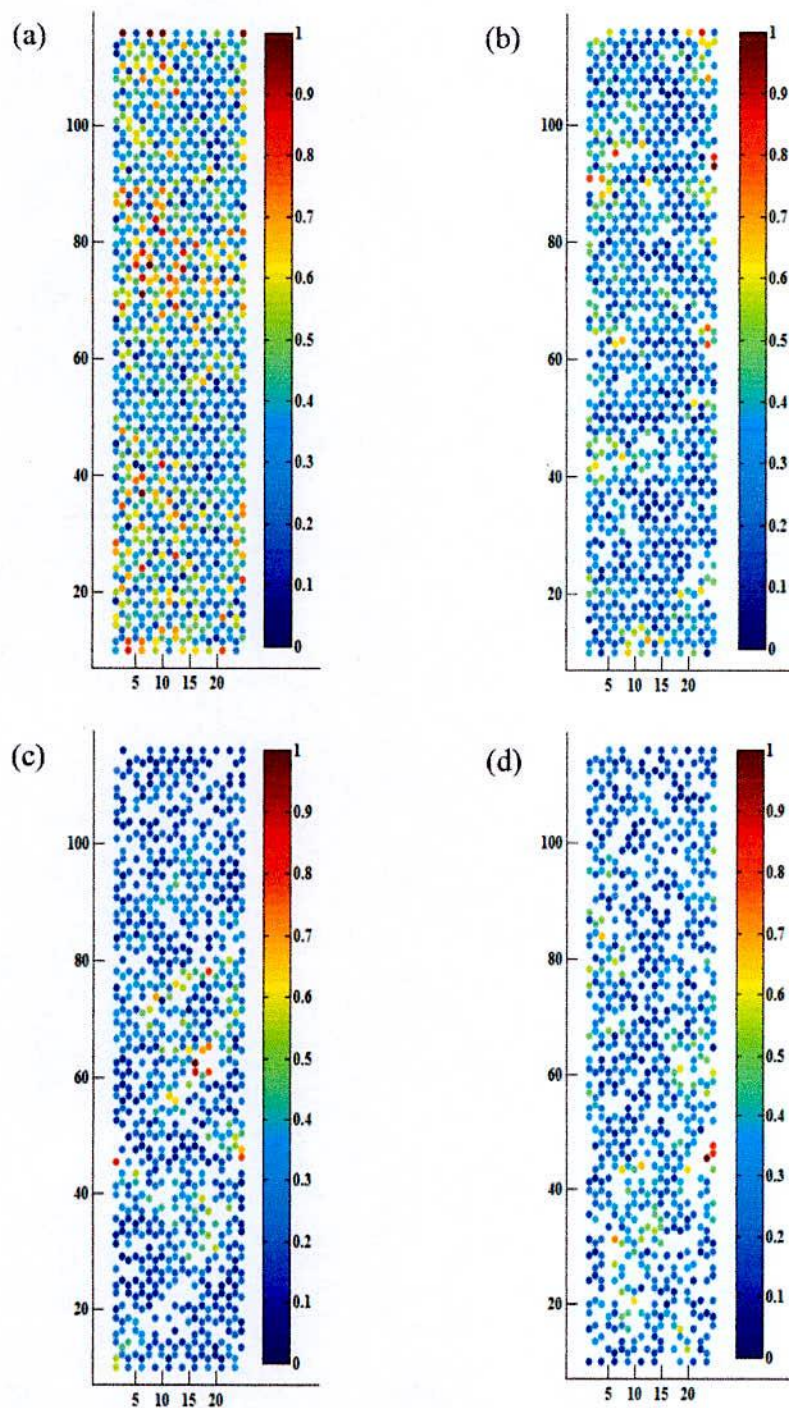


Figure 4.6 : Typical mode pattern of (a) pristine (b) 10% vacancy (c) 20% vacancy and (d) 30% vacancy induced (10,0) CNT. Each circle denotes an atom and the colors denote the displacement, which is linearly normalized. The vertical and horizontal axis are scaled in angstrom unit.

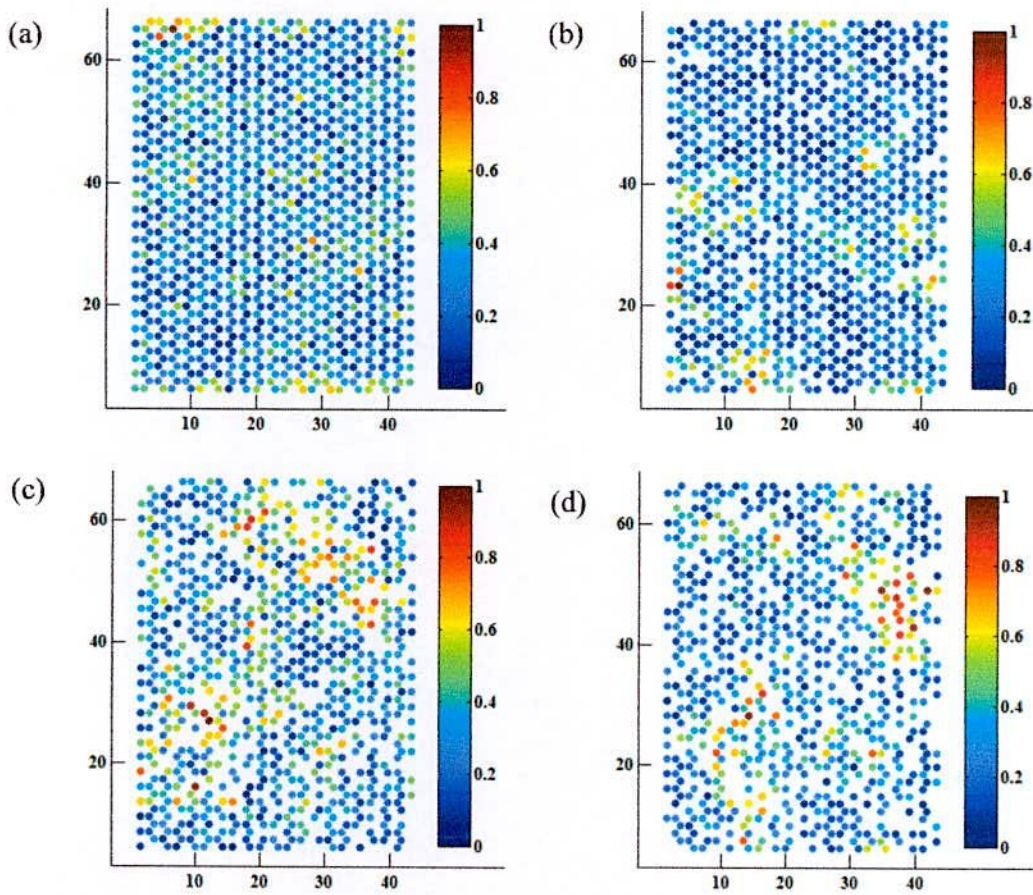


Figure 4.7 : Typical mode pattern of (a) pristine (b) 10% vacancy (c) 20% vacancy and (d) 30% vacancy induced (10,10) CNT. Each circle denotes an atom and the colors denote the displacement, which is linearly normalized. The vertical and horizontal axis are scaled in angstrom unit.

If vacancies are present in those crystal system phonons are confined to a particular region. Due to breakdown of momentum conservation of a periodic arrangement of atoms, phonons are scattered into other phonon states. In this case phonon wave vectors are no longer good quantum numbers that means they are localized in real space. To observe localization property in defective CNT, particularly, emphasis on D-band of phonon modes has given. D mode is originated from iTO phonon at the K points on the Brillouin zone boundary. Generally D mode appears if there is any breakdown of the in-plane translational symmetry because of vacancies or finite size effects. D-band frequency is a strong feature in defective CNT, because double-resonance scattering process requires defects for momentum conservation. D-band frequency is also curvature sensitive. It decreases with increasing curvature [92-14]. In

Figures 4.5(a) and 4.5(b), it is shown the vibrational direction of D-band mode for defective (10,0) and (10,10) CNTs. Here we see a strong localization effect and very few atoms are vibrating (red arrows) near defects. It is also observed that less number of atoms are vibrating in (10,0) CNT than (10,10) CNT and this implies that the localization effect is stronger in (10,0) CNT than (10,10) CNT. This also indicates that the localization effect depends on curvature effect. As curvature softens carbon-carbon bond strength and it can be predicted that this fact influences on phonon localization in defective (10,0) ZCNT.

To visualize more elaborately the localization effect in defective CNTs, I represent the typical mode pattern of the perfect unfolded CNTs associated with different types of disordered unfolded CNTs at 1350 cm^{-1} . I use a total of 1000 lattice spaces because the vibrational modes show strong localization within this range of lattice spaces. Therefore, it is not necessary to have a large number of lattice spaces. In Figure 4.6 each circle denotes an atom and the color denotes the displacement. In Figure 4.6(a) mode pattern of perfect (10,0) ZCNT is shown. Here we see that all modes are almost perfectly distributed all over the lattice spaces Figure 4.6(b) shows a mode pattern for 10% atomic vacancy. This figure depicts that when vacancies are induced in the perfect crystal system, all modes are no longer well distributed. Some modes become localized. Figure 4.6(c) shows the more strong localization effect with 20% atomic vacancies. In Figure 4.6(d), it is observed very strong localization with only two or three atoms are vibrating with the largest amplitude in a particular region for 30% defect density. This strong localization is the resultant of the resonant vibration of the randomly distributed atoms in the percolation network of defective (10,0) CNT. As the centers of the localized modes change its position with different time development, I have applied a random force to each atom of the crystal system to extract the eigenmodes. Although the localization center moves with the time development, in all time development it stays asymmetrically around the atomic vacancies. Here it is observed that localization effect increases with increasing defect densities and this effect is stronger specially near the vacancies. I have also calculated mode patterns of (10,10) ACNT, which are shown in Figure 4.7. In Figure 4.7(a), it is observed extended mode pattern for pristine (10,10) CNT sample. Figures 4.7(b), 4.7(c) and 4.7(d) illustrate a mode pattern for 10%, 20% and 30% defect densities of (10,10) CNT respectively. Here it is also found that with increasing defect densities localization effect becomes severe. Simulated values of References 95 and 96 show

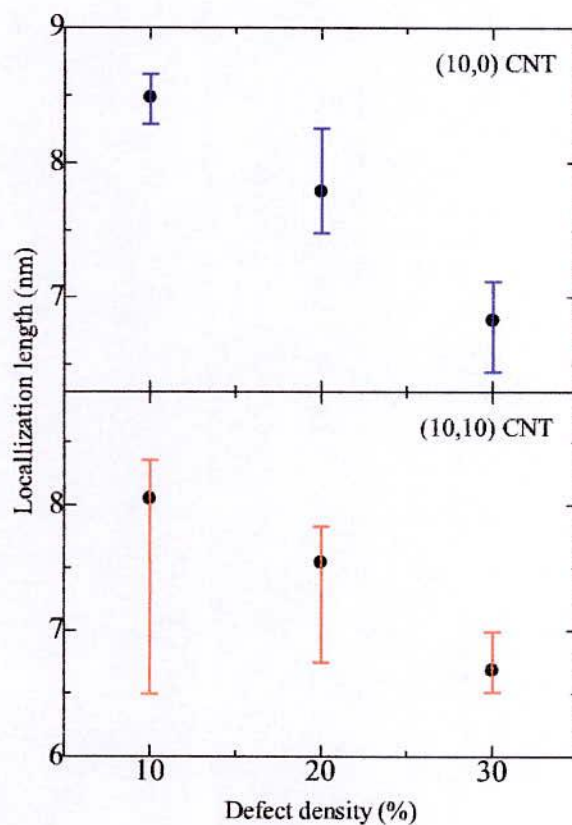


Figure 4.8 : Localization length as a function of defect density for both (10,0) and (10,10) CNTs.

that thermal conductivity of CNT decreases with increasing vacancy type defects. Their findings are completely agreed with these findings. As phonons are the carrier of thermal energy, it is seen that with increasing defect densities phonons are become strongly localized near vacancy sites, which reduces thermal conductivity. Furthermore, it does not observe any edge phonon localization as found in some previous works [87] for graphene nanoribbon, because I have used PBC along the chiral vector direction of CNT. Thus no edge phonon localization effect is found.

4.4 Localization Length of SWCNT

Finally, I have calculated phonon localization length for (10,0) and (10,10) as a function

of defect density as shown in Figure 4.8. The simulation performed for K point iTO phonon mode at $\omega=1350 \text{ cm}^{-1}$ for 10,000 atoms. The Defect density is varied from 10% to 30%. The filled circles are obtained by averaging over 10 eigenmodes, because the localization length shows large fluctuations in values. To determine the localization length I first obtain an inverse participation ratio (IPR_λ). It is previously stated that value of IPR_λ varies from 1 to $1/N$. As the localization length is inversely proportional to the square root of IPR_λ , it should be obtained lowest localization length for strong localization. From Figure 4.8, it is clearly shown that the localization length decreases for both (10,0) and (10,10) CNTs with increasing defect densities. I have found localization lengths are larger in value for same defect density in (10,0) CNT than (10,10) CNT, which is expected due to curvature effect. This simulation results for localization length are well agreed with the results of the previous works on graphene, because the characteristics of graphene are transferable to the carbon nanotube [86]. As we know that localized states are obtained mainly when mode energy is spatially concentrated at the defect sites. There may other factors behind this effect. In optical high-frequency region, defect induced backscattering effect become significant to create localized states. The localized states are also comparable to the formation of the island that vibrates at a different frequency from the rest of the crystal lattice.

CHAPTER V

Summary and Outlook

5.1 Conclusion

It is carried out an in-depth and systematic numerical experiment on phonon property of pristine and vacancy induced SWCNTs. This experiment consists of two types of CNTs, semiconducting (10,0) ZCNT and metallic (10,10) ACNT. The forced vibrational method which is very suitable to treat large and disordered crystal system has been attributed to inspect vibrational eigenmodes of defective CNTs. We have examined the effect of vacancies and curvature on PDOS as well as on localization effect of CNT.

The simulated PDOS also shows some extraordinary character about PDOSs with respect to pristine sample in defective situation. We have found strong dependency of Raman active E_{2g} mode on vacancy type defects and curvature for both types of CNTs. The E_{2g} mode found from our simulation at 1576 cm^{-1} and 1581 cm^{-1} for (10,0) and (10,10) CNTs respectively. The E_{2g} mode shows linear reduction towards lower frequency region with increasing defect densities and curvature of CNTs. It is found that E_{2g} mode softening effect is stronger in (10,0) than (10,10) CNT due to curvature effect. Our experimental values shows that for vacancy concentrations of 10% or higher, the E_{2g} peak has been reduced into a shoulder or it has been completely disappeared. Some fine structures have been vanished, although some sharp peaks have appeared with increasing vacancy concentrations. We have found some fine peaks in the low-frequency region with the increase in defect density in PDOS of both CNTs.

The dependency of the phonon localization effect on vacancy-type defects and curvature has elaborately interpreted with visualizing mode pattern and determining the localization length at D-band high optical frequency for in-plane transverse optical phonon mode at the K points of Brillouin zone. We have found reduction of localization length with increasing defect densities. We have observed a stronger localization effect in (10,0) CNT than (10,10) CNT due to curvature effect.

Finally from lattice vibrational view point, these findings are not only important in fundamental science of CNT, but also in advanced nanoelectronics, where the non-ideal vacancy induced CNTs affect the electron transport properties significantly.

5.2 Future Outlooks

The model developed in this dissertation has proven to accurately describe the vibrational properties of disordered 1D SWCNT. At the same time, there have been several important issues in the field that remain to be addressed. These include further investigation of many body interactions and electron phonon scattering effects, quantitative analysis of isotopic, doping, hydrogen passivation defects and specific structural defects such as Stone-Walse defects in SWCNT samples, and anharmonic effects responsible for the thermal conductivity in the SWCNT. The effect of phonon localization on the electron localization can be investigated elaborately. From these calculations it was shown that localized vibrational modes are moving in nature with different time development. A more detailed study can be performed to determine the exact relationship of localized eigenvectors for various types of defects with different concentrations.

REFERENCES

- 1 E. Pop, D. Mann, Q. Wang, K. Goodson and H. Dai, 2006, "Thermal conductance of an individual single-wall carbon nanotube above room temperature", *Nano Letters*, Vol. 6, pp. 96-100.
- 2 S. Hong and S. Myung, 2007, "Nanotube electronics: A flexible approach to mobility", *Nature Nanotechnology*, Vol. 2, pp. 207-208.
- 3 M. Haque, C. Marinelli, F. Udrea, and W. Milne, 2006, "Absorption characteristics of single wall carbon nanotubes", *NSTI-Nanotech*, Vol. 1, pp. 134-137.
- 4 Y. I. Jhon, C. Kim, M. Seo, W. J. Cho, S. Lee and Y. M. Jhon, 2016, "Tensile characterization of single-walled carbon nanotubes with helical structural defects", *Scientific Reports*, Vol. 6, pp. 20324.
- 5 Z. Spitalsky, D. Tasis, K. Papagelis and C. Galiotis, 2010, "Carbon nanotube-polymer composites: chemistry, processing, mechanical and electrical properties", *Progress in Polymer Science*, Vol. 35, pp. 357-401.
- 6 X. Wang, Q. Li, J. Xie, Z. Jin, J. Wang, Y. Li, K. Jiang and S. Fan, "Fabrication of ultralong and electrically uniform single-walled carbon nanotubes on clean substrates", *Nano Letters*, Vol. 9, pp. 3137-3141.
- 7 R. Martel, T. Schmidt, H. Shea, T. Hertel and P. Avouris, 1998, "Single- and multi-wall carbon nanotube field-effect transistors", *Applied Physics Letters*, Vol. 73, pp. 2447-2449.
- 8 J. U. Lee, 2005, "Photovoltaic effect in ideal carbon nanotube diodes", *Applied Physics Letters*, Vol. 87, pp. 073101.
- 9 Z. Wu, Z. Chen, X. Du, J. M. Logan, J. Sippel, M. Nikolou, K. Kamaras, J. R. Reynolds, D. B. Tanner and A. F. Hebard et al., 2004, "Transparent, conductive carbon nanotube films", *Science*, Vol. 305, pp. 1273-1276.
- 10 M. W. Rowell, M. A. Topinka, M. D. McGehee, H.-J. Prall, G. Dennler, N. S. Sariciftci, L. Hu and G. Gruner, 2006, "Organic solar cells with carbon nanotube network electrodes", *Applied Physics Letters*, Vol. 88 pp. 233506.
- 11 H. Li and K. Banerjee, 2009, "High-frequency analysis of carbon nanotube interconnects and implications for on-chip inductor design", *IEEE Transactions on Electron Devices*, Vol. 56, pp. 2202-2214.
- 12 S. Ng, J. Wang, Z. Guo, J. Chen, G. Wang and H. K. Liu, 2005, "Single wall carbon nanotube paper as anode for lithium-ion battery", *Electrochimica Acta*, Vol. 51, pp. 23-28.
- 13 B. L. Allen, P. D. Kichambare and A. Star, 2007, "Carbon nanotube field-effect transistor-based biosensors", *Advanced Materials*, Vol. 19, pp. 1439-1451.

- 14 W. Choi, D. Chung, J. Kang, H. Kim, Y. Jin, I. Han, Y. Lee, J. Jung, N. Lee and G. Park, et al., 1999, "Fully sealed, high-brightness carbon-nanotube field emission display, Applied Physics Letters, Vol. 75, pp. 3129-3131.
- 15 www.grandviewresearch.com.
- 16 P. Zarabadi-Poor and A. Badiei, 2011, "Synthesis of carbon nanotubes using metal modified nanoporous silicas", Carbon Nanotubes-Growth and Applications, M. Naraghi (Ed.), Chap 3, pp. 59, InTech, 1st Ed.
- 17 N. Nemeč, D. Tomanek and G. Cuniberti, 2006, "Contact dependence of carrier injection in carbon nanotubes: an ab initio study", Physical Review Letters, Vol. 96, pp. 076802.
- 18 N. Nemeč, D. Tomanek and G. Cuniberti, 2008, "Modeling extended contacts for nanotube and graphene devices", Physical Review B, Vol. 77, pp. 125420.
- 19 N. Nemeč, K. Richter and G. Cuniberti, 2008, "Diffusion and localization in carbon nanotubes and graphene nanoribbons", New Journal of Physics, Vol. 10, pp. 065014.
- 20 S. Krompiewski, R. Gutierrez and G. Cuniberti, 2004, "Giant magneto resistance of multiwall carbon nanotubes: Modeling the tube/ferromagnetic-electro deburying contact", Physical Review B, Vol. 69, pp. 155423.
- 21 A. A. Balandin, S. Ghosh, W. Bao, I. Calizo, D. Teweldebrhan, F. Miao and C. N. Lau, 2008, "Superior thermal conductivity of single-layer graphene", Nano Letters, Vol. 8, pp. 902-907.
- 22 M. Gheorghe, R. Gutierrez, N. Ranjan, A. Pecchia, A. Di Carlo and G. Cuniberti, 2005, "Vibrational effects in the linear conductance of carbon nanotubes", Europhysics Letters, Vol. 7, pp. 438.
- 23 S. Berber, Y.-K. Kwon and D. Tomanek, 2000, "Unusually high thermal conductivity of carbon nanotubes", Physical Review Letters, Vol. 84, pp. 4613.
- 24 K. Saito, J. Nakamura and A. Natori, 2007, "Ballistic thermal conductance of a graphene sheet", Physical Review B, Vol. 76, pp. 115409.
- 25 L. X. Benedict, S. G. Louie and M. L. Cohen, 1996, "Heat capacity of carbon nanotubes", Solid State Communications, Vol. 100, pp. 177-180.
- 26 U. Kim, X. Liu, C. Furtado, G. Chen, R. Saito, J. Jiang, M. Dresselhaus and P. Eklund, 2005, "Infrared-active vibrational modes of single-walled carbon nanotubes", Physical Review Letters, Vol. 95, pp. 157402.
- 27 A. C. Ferrari, J. Meyer, V. Scardaci, C. Casiraghi, M. Lazzeri, F. Mauri, S. Piscanec, D. Jiang, K. Novoselov and S. Roth, et al., 2006, "Raman spectrum of graphene and graphene layers", Physical Review Letters, Vol. 97, pp. 187401.

- 28 A. Rao, E. Richter, S. Bandow, B. Chase, P. Eklund, K. Williams, S. Fang, K. Subbaswamy, M. Menon and A. Thess, et al., 1997, "Diameter-selective Raman scattering from vibrational modes in carbon nanotubes", *Science*, Vol. 275, pp. 187-191.
- 29 L. Woods and G. Mahan, 2000, "Electron-phonon effects in graphene and armchair (10, 10) single-wall carbon nanotubes", *Physical Review B*, Vol. 61, pp. 10651.
- 30 O. Dubay and G. Kresse, 2003, "Accurate density functional calculations for the phonon dispersion relations of graphite layer and carbon nanotubes", *Physical Review B*, Vol. 67, pp. 035401.
- 31 S. Piscanec, M. Lazzeri, F. Mauri, A. Ferrari and J. Robertson, 2004, "Kohn anomalies and electron-phonon interactions in graphite", *Physical Review Letters*, Vol. 93, pp. 185503.
- 32 K.-P. Bohnen, R. Heid, H. Liu and C. Chan, 2004, "Lattice dynamics and electron phonon interaction in (3, 3) carbon nanotubes", *Physical Review Letters*, Vol. 93, pp. 245501.
- 33 M. Lazzeri, S. Piscanec, F. Mauri, A. Ferrari and J. Robertson, 2005, "Electron transport and hot phonons in carbon nanotubes", *Physical Review Letters*, Vol. 95, pp. 236802.
- 34 R. Gutierrez, S. Mohapatra, H. Cohen, D. Porath and G. Cuniberti, 2006, "In elastic quantum transport in a ladder model: Implications for dna conduction and comparison to experiments on suspended dna oligomers", *Physical Review B*, Vol. 74, pp. 235105.
- 35 N. Bonini, M. Lazzeri, N. Marzari and F. Mauri, 2007, "Phonon anharmonicities in graphite and graphene", *Physical Review Letters*, Vol. 99, pp. 176802.
- 36 H. Suzuura and T. Ando, 2002, "Phonons and electron-phonon scattering in carbon nanotubes", *Physical Review B*, Vol. 65, pp. 235412.
- 37 E. Mariani and F. von Oppen, 2008, "Flexural phonons in free-standing graphene", *Physical Review Letters*, Vol. 100, pp. 076801.
- 38 Z. Tang, L. Zhang, N. Wang, X. Zhang, G. Wen, G. Li, J. Wang, C. Chan and P. Sheng, 2001, "Superconductivity in 4 angstrom single-walled carbon nanotubes", *Science*, Vol. 292, pp. 2462-2465.
- 39 K.-i. Sasaki, H. Farhat, R. Saito and M. S. Dresselhaus, 2010, "Kohn anomaly in Raman spectroscopy of single wall carbon nanotubes", *Physica E*, Vol. 42, pp. 2005-2015.
- 40 S. Piscanec, M. Lazzeri, J. Robertson, A. C. Ferrari and F. Mauri, 2007, "Optical phonons in carbon nanotubes: Kohn anomalies, peierls distortions, and dynamic effects", *Physical Review B*, Vol. 75, pp. 035427
- 41 P. G. Collins, 2010, "Defects and disorder in carbon nanotubes", *Oxford Handbook of Nanoscience and Technology: Materials: Structures, Properties and Characterization*

Techniques, Vol. 2, pp. 31.

- 42 A. Maradudin, 1966, "Theoretical and experimental aspects of the effects of point defects and disorder on the vibrations of crystals 1", *Solid State Physics*, Vol. 18, pp. 273-420.
- 43 A. Maradudin, 1967, "Theoretical and experimental aspects of the effects of point defects and disorder on the vibrations of crystals 2", *Solid State Physics*, Vol. 19, pp. 1-134.
- 44 J. Kurti, V. Zolyomi, A. Gruneis and H. Kuzmany, 2002, "Double resonant Raman phenomena enhanced by van hove singularities in single-wall carbon nanotubes", *Physical Review B*, Vol. 65, pp. 165433.
- 45 J. Yu, R. Kalia and P. Vashishta, 1995, "Phonons in graphitic tubules", *Europhysics Letters*, Vol. 32, pp. 43.
- 46 D. Sanchez-Portal, E. Artacho, J. M. Soler, A. Rubio and P. Ordejon, 1999, "Ab initio structural, elastic, and vibrational properties of carbon nanotubes", *Physical Review B*, Vol. 59, pp. 12678.
- 47 L.-H. Ye, B.-G. Liu, D.-S. Wang and R. Han, 2004, "Ab initio phonon dispersions of single-wall carbon nanotubes", *Physical Review B*, Vol. 69, pp. 235409.
- 48 R. Saito, T. Takeya, T. Kimura, G. Dresselhaus and M. Dresselhaus, 1998, "Raman intensity of single-wall carbon nanotubes", *Physical Review B*, Vol. 57, pp. 4145.
- 49 M. L. Williams and H. J. Maris, 1985, "Numerical study of phonon localization in disordered systems", *Physical Review B*, Vol. 34, pp. 4508.
- 50 N. N. Greenwood and A. Earnshaw, 1997, "Chemistry of the Elements", Elsevier, 2nd. Ed.
- 51 www.webelements.com.
- 52 T. W. Odom, J.-L. Huang, P. Kim and C. M. Lieber, 1998, "Atomic structure and electronic properties of single-walled carbon nanotubes", *Nature*, Vol. 391, pp. 62-64.
- 53 K. S. Novoselov, A. K. Geim, S. V. Morozov, D. Jiang, Y. Zhang, S. V. Dubonos, I. V. Grigorieva and A. A. Firsov, 2004, "Electric field effect in atomically thin carbon films", *Science*, Vol. 306, pp. 666-669.
- 54 S. Iijima, 1991, "Helical microtubules of graphitic carbon", *Nature*, Vol. 354, pp. 56-58.
- 55 S. Iijima and T. Ichihashi, "Single-shell carbon nanotubes of 1-nm diameter", 1993, Vol. 363, pp. 603.

- 56 D. Bethune, C. Klang, M. De Vries, G. Gorman, R. Savoy, J. Vazquez and R. Beyers, 1993, "Cobalt-catalysed growth of carbon nanotubes with single atomic-layer walls", *Nature*, Vol. 363, pp. 605-607.
- 57 H. W. Kroto, J. R. Heath, S. C. O'Brien, R. F. Curl and R. E. Smalley, "C60: Buckminsterfullerene", *Nature*, Vol. 318, pp. 162-163.
- 58 M. S. Islam, 2014, "Vibrational properties of disordered graphene and related 2d materials", University of Fukui.
- 59 A. Jorio, M. Dresselhaus, R. Saito and G. Dresselhaus, 2011, "Raman spectroscopy in graphene related systems", WILEY-VCH Verlag GmbH & Co. KGaA.
- 60 J. Lee and B. Lee, 2012, "Modal analysis of carbon nanotubes and nanocones using fem", *Computational Materials Science*, Vol. 51, pp. 30-42.
- 61 C. -H. Liu, Y.-Y. Liu, Y.-H. Zhang, R. -R. Wei, H. -L. Zhang, 2009, "Tandem extraction strategy for separation of metallic and semiconducting SWCNTs using condensed benzenoid molecules: Effects of molecular morphology and solvent", *Physical Chemistry Chemical Physics*, Vol. 11, pp. 7257-67.
- 62 M. Dresselhaus, G. Dresselhaus and R. Saito, 1995, "Physics of carbon nanotubes", *Carbon*, Vol. 33, pp. 883-891.
- 63 R. Saito, G. Dresselhaus and M. S. Dresselhaus, 1998, "Physical properties of carbon nanotubes", World Scientific.
- 64 R. Jishi, L. Venkataraman, M. Dresselhaus and G. Dresselhaus, 1993, "Phonon modes in carbon nanotubes", *Chemical Physics Letters*, Vol. 209, pp. 77-82.
- 65 M. Dresselhaus, G. Dresselhaus, A. Jorio, A. Souza Filho and R. Saito, 2002, "Raman spectroscopy on isolated single wall carbon nanotubes", *Carbon*, Vol. 40, pp. 2043-2061.
- 66 M. Damnjanovic, I. Milosevic, T. Vukovic and R. Sredanovic, 1999, "Full symmetry, optical activity, and potentials of single-wall and multi-wall nanotubes", *Physical Review B*, Vol. 60, pp. 2728.
- 67 M. Damnjanovic, I. Milosevic, T. Vukovic and R. Sredanovic, 1999, "Symmetry and lattices of single-wall nanotubes", *Journal of Physics A*, Vol. 32, pp. 4097.
- 68 S. Reich, C. Thomsen and J. Maultzsch, 2008, "Carbon nanotubes: basic concepts and physical properties", John Wiley & Sons.
- 69 S. Reich, C. Thomsen and P. Ordejon, 2001, "Phonon eigenvectors of chiral nanotubes", *Physical Review B*, Vol. 64, pp. 195416.

- 70 A. Fainstein, P. Etchegoin, M. Chamberlain, M. Cardona, K. T. Otemeyer and K. Eberl, 1995, "Selection rules and dispersion of gaas/alas multiple-quantumwell optical phonons studied by Raman scattering in right-angle, forward and backscattering in-plane geometries", *Physical Review B*, Vol. 51, pp. 14448.
- 71 B. Jusserand and M. Cardona, 1989, "Raman spectroscopy of vibrations in super lattices, in: *Light Scattering in Solids V*", pp. 49-152, Springer.
- 72 J. Kurti, V. Zolyomi, M. Kertesz and G. Sun, 2003, "The geometry and the radial breathing mode of carbon nanotubes: beyond the ideal behavior", *New Journal of Physics*, Vol. 5, pp. 125.
- 73 E. Dobardzic, I. Milosevic, B. Nikolic, T. Vukovic and M. Damnjanovic, 2003, "Single-wall carbon nanotubes phonon spectra: Symmetry-based calculations", *Physical Review B*, Vol. 68, pp. 045408.
- 74 M. Damnjanovic, E. Dobardzic and I. Milosevic, 2004, "Chirality dependence of the radial breathing mode: a simple model", *Journal of Physics: Condensed Matter*, Vol. 16, pp. L505.
- 75 P. Eklund, J. Holden and R. Jishi, 1995, "Vibrational modes of carbon nanotubes; spectroscopy and theory", *Carbon*, Vol. 33, pp. 959-972.
- 76 K. Iakoubovskii, N. Minami, T. Ueno, S. Kazaoui and H. Kataura, 2008, "Optical characterization of double-wall carbon nanotubes: evidence for inner tube shielding", *The Journal of Physical Chemistry C*, Vol. 112, pp. 11194-11198.
- 77 F. Wegner, 1980, "Inverse participation ratio in $2+\epsilon$ dimensions", *Zeitschrift fur Physik B*, Vol. 36, pp. 209-214.
- 78 B. Kramer and A. MacKinnon, 1993, "Localization: theory and experiment", *Reports on Progress in Physics*, Vol. 56, pp. 1469.
- 79 S. Datta, 2005, "Quantum transport: atom to transistor", Cambridge University Press.
- 80 V. K. S. Shante and S. Kirkpatrick, 2006, "An introduction to percolation theory", *Advances in Physics*, Vol. 20, pp. 325-357.
- 81 www.scienceforeveryone.com
- 82 Z. V. Djordjevic, H. E. Stanley and A. Margolina, 1982, "Site percolation threshold for honeycomb and square lattices", *Journal of Physics A*, Vol. 15, pp. L405-L412.
- 83 P. Avouris, Z. Chen and V. Perebeinos, 2007, "Carbon-based electronics", *Nature Nanotechnology*, Vol. 2, pp. 605-615.

- 84 M. Dresselhaus and P. Eklund, 2000, "Phonons in carbon nanotubes", *Advances in Physics*, Vol. 49, pp. 705-814.
- 85 R. Saito, M. Hofmann, G. Dresselhaus, A. Jorio and M. Dresselhaus, 2011, "Raman spectroscopy of graphene and carbon nanotubes", *Advances in Physics*, Vol. 60, pp. 413-550.
- 86 M. S. Islam, K. Ushida, S. Tanaka and A. Hashimoto, 2013, "Numerical experiments on phonon properties of isotope and vacancy-type disordered graphene", *Diamond and Related Materials*, Vol. 40, pp. 115-122.
- 87 M. S. Islam, K. Ushida, S. Tanaka and A. Hashimoto, 2013, "Numerical analysis on vacancy induced vibrational properties of graphene nanoribbons", *Computational Materials Science*, Vol. 79, pp. 356-361.
- 88 N. Mingo and D. Broido, 2005, "Length dependence of carbon nanotube thermal conductivity and the problem of long waves", *Nano Letters*, Vol. 5, pp. 1221-1225.
- 89 C. Sevik, H. Sevincli, G. Cuniberti and T. Cagin, 2011, "Phonon engineering in carbon nanotubes by controlling defect concentration", *Nano letters*, Vol. 11, pp. 4971-4977.
- 90 G. Mahan and G. S. Jeon, 2004, "Flexure modes in carbon nanotubes", *Physical Review B*, Vol. 70, pp. 075405.
- 91 H. Ochoa, E. V. Castro, M. Katsnelson and F. Guinea, 2012, "Scattering by flexural phonons in suspended graphene under back gate induced strain", *Physica E*, Vol. 44, pp. 963-966.
- 92 M. A. Pimenta, A. Jorio, S. D. Brown, A. G. Souza Filho, G. Dresselhaus, J. Hafner, C. Lieber, R. Saito and M. Dresselhaus, 2001, "Diameter dependence of the raman D-band in isolated single-wall carbon nanotubes", *Physical Review B*, Vol. 64, pp. 041401.
- 93 A. Souza Filho, A. Jorio, G. G. Samsonidze, G. Dresselhaus, M. Pimenta, M. Dresselhaus, A. K. Swan, M. Unlu, B. Goldberg and R. Saito, 2003, "Competing spring constant versus double resonance effects on the properties of dispersive modes in isolated single-wall carbon nanotubes", *Physical review B*, Vol. 67, pp. 035427.
- 94 A. Jorio et al., 2004, "Advances in single nanotube spectroscopy: Raman spectra from cross-polarized light and chirality dependence of raman frequencies", *Carbon*, Vol. 42, pp. 1067-1069.
- 95 J. Che, T. Cagin and W. A. Goddard III, 2000, "Thermal conductivity of carbon nanotubes", *Nanotechnology*, Vol. 11, pp. 65.
- 96 F. Dai-Li, F. Yan-Hui, C. Yang, L. Wei and Z. Xin-Xin, 2013, "Effects of doping, stonewales and vacancy defects on thermal conductivity of single-wall carbon nanotubes", *Chinese Physics B*, Vol. 22, pp. 016501.

List of Publications

1. Ashraful Hossain Howlader, Md. Sherajul Islam, Satoru Tanaka, Takayuki Makino and Akihiro Hashimoto, 2018, "Vacancy and Curvature Effects on the Phonon Properties of Single Wall Carbon Nanotube", Jpn. J. Apl. Phy. Vol. 57. pp. 02CB08.
 2. Ashraful Hossain Howlader, Md. Sherajul Islam, Md. Rafiqul Islam and Ashraful Ghani Bhuiyan, June 18-21, 2017, "Vacancy Induced Phonon Properties of Single Wall Carbon Nanotube", The 6th International Symposium on Organic and Inorganic Electronic Materials and Related Nanotechnologies (EM-NANO 2017), Fukui, Japan.
-